

MASTER

Advanced numerical techniques for the multi-scale modelling of non-linear dynamic metamaterials

Castricum, B.A.

Award date:
2021

[Link to publication](#)

Disclaimer

This document contains a student thesis (bachelor's or master's), as authored by a student at Eindhoven University of Technology. Student theses are made available in the TU/e repository upon obtaining the required degree. The grade received is not published on the document as presented in the repository. The required complexity or quality of research of student theses may vary by program, and the required minimum study period may vary in duration.

General rights

Copyright and moral rights for the publications made accessible in the public portal are retained by the authors and/or other copyright owners and it is a condition of accessing publications that users recognise and abide by the legal requirements associated with these rights.

- Users may download and print one copy of any publication from the public portal for the purpose of private study or research.
- You may not further distribute the material or use it for any profit-making activity or commercial gain



Department of Mechanical Engineering
Mechanics of Materials

Advanced numerical techniques for the multi-scale modelling of non-linear dynamic metamaterials

Thesis

Student:

B.A. CASTRICUM
1270729

Supervisors:

dr. ir. V.G. KOUZNETSOVA
ir. T.F.W. van NULAND

March 17, 2021

Abstract

Metamaterials are gaining popularity due to their interesting properties and many potential applications. Locally resonant acoustic metamaterials is one of these materials. Locally resonant acoustic metamaterials have frequency ranges where waves do not propagate, known as ‘band gaps’. Research has been performed to accurately predict the properties of these materials. A computational homogenization framework is used to efficiently predict the properties. However, when non-linear material models are used, discrepancies are found. These discrepancies are linked to the used implicit time integration scheme.

In this work, the influence of the implicit time integration scheme is analysed. Also, different implicit time integration schemes are considered. The properties of the implicit time integration schemes are compared and analysed in a benchmark problem.

The time integration schemes are implemented in the computational homogenization framework. Some time integration schemes consists of multiple sub steps within a time step. These schemes require additional care in the homogenization framework. The framework is compared to direct numerical simulations for three different constitutive models of the local resonator; linear elastic, cubic and Neo-Hookean. In the case of linear locally resonant acoustic metamaterials, the time integration schemes predict similar results for the displacement. For high homogenization levels, the influence of the spatial discretization has the largest contribution to discrepancies shown in the results. The use of a different time integration scheme does not translate in more accurate results.

In the case of non-linear locally resonant acoustic metamaterials, the same can be concluded; the use of a different time integration scheme does not translate to an increase in accuracy.

Contents

1	Introduction	7
1.1	Project aim and goals	8
1.2	Structure of this report	8
2	Time integration	9
2.1	Time integration schemes	9
2.1.1	Integration scheme selection	12
2.2	The basic equations of time integration	13
2.2.1	Trapezoidal rule	14
2.2.2	Bathe scheme	15
2.2.3	Wen scheme	15
2.2.4	Kim scheme	16
2.2.5	Li scheme	16
3	Benchmark problem	17
3.1	Discussion	20
4	Numerical model	24
4.1	Direct numerical simulation	24
4.2	Computational homogenization simulations	26
4.2.1	Macroscopic problem	26
4.2.2	Microscopic problem	27
4.2.3	Macroscopic stress, momentum and tangents	28
4.3	Constitutive relations	29
4.3.1	Linear elastic	29
4.3.2	Cubic	29
4.3.3	Neo-Hookean	30
4.4	Boundary conditions for composite time integration schemes	30
4.5	Time integration scheme on the microscopic scale	31
4.6	Simulation approach	32
5	Direct numerical simulations	33
5.1	Linear constitutive model	33
5.2	Cubic constitutive model	36
5.3	Neo-Hookean constitutive model	38
5.4	Discussion	40
6	Computational homogenization simulations	42
6.1	Linear Elastic	42
6.2	Cubic	44
6.3	Neo-Hookean	46
6.4	Quadratic elements	47

6.5 Discussion	49
7 Conclusions and recommendations	50
8 Appendix A: Finite element method	55

Nomenclature

Symbols

\dot{a}	first time derivation	
A	amplitude	[m]
a	scalar	
\ddot{a}	second time derivation	
\mathbf{a}	vector	
b	integration constant for Bathe scheme	[-]
A	matrix	
$\mathbf{a} \cdot \mathbf{b}$	inner product	
B	root mean square displacement	[m]
A:B	inner product	
${}^2\mathbf{A}$	second-order tensor	
c	wave speed	[m/s]
A^T	conjugation	
${}^3\mathbf{A}$	third-order tensor	
c_1, c_2, c_3	integration constants	[-]
Δ	finite variation	
${}^4\mathbf{A}$	fourth-order tensor	
C_{10}	Neo-Hookean material parameter	[N/m ²]
${}^4\mathbf{C}_M^{(1)}, {}^3\mathbf{C}_M^{(2)}, {}^3\mathbf{C}_M^{(3)}, {}^2\mathbf{C}_M^{(4)}$		[N/m ²], [N/m ³], [N/m ³], [N/m ⁴]
∇	gradient operator	
d	diameter of lead core	[m]
d_0, d_1, d_2, d_3, d_4	integration constants	[-]
e	engineering strain	[-]
E	Young's modulus	[N/m ²]

f_{ext}	external nodal forces	[N]
f_{int}	internal nodal forces	[N]
F	deformation gradient tensor	[-]
h	amount of homogenization	[-]
k	wavenumber	[1/m]
k_e	nodal stiffness	[N/m]
K	stiffness matrix	[N/m]
$\hat{\mathbf{K}}$	iteration matrix	[N/m]
l	length	[m]
M	mass matrix	[kg]
n_T	number of time steps	[-]
N	shape functions	[-]
$\dot{\mathbf{p}}_0$	momentum rate	[N/m ³]
P	first Piola-Kirchoff stress	[N/m ²]
r	residual	[N]
\mathbf{R}	external nodal forces	[N]
$\hat{\mathbf{R}}$	external forces based iteration matrix	[N]
S	acceleration based iteration matrix	[N/m]
t	time	[s]
t_c	thickness of rubber coating	[m]
t	tractions	[N/m ²]
Δt	time step	[s]
u	displacement	[m]
\dot{u}	velocity	[m/s]
\ddot{u}	acceleration	[m/s ²]
V	volume	[m ³]
x	position	[m]
X_0	position with respect to undeformed configuration	[m]
X_{0m}^a	arbitrary microscopic position vector	[m]
X_{0m}^r	reference microscopic position vector	[m]
w	integration constant for Wen scheme	[-]
α	degree of cubic non-linearity	[-]

β, γ	time integration parameters	[-]
Γ	volume boundary	[m ²]
λ	stretch	[-]
Λ	wavelength	[m]
ν	Poisson's ratio	[-]
τ	time integration parameter	[-]
ρ	density	[kg/m ³]
ω	frequency	[1/s]
σ	Cauchy stress	[N/m ²]
θ	transmission ratio	[-]

Sub or superscripts

*	tied degree of freedom
0	undeformed or initial state
a	arbitrary
f	free degree of freedom
m	microscopic quantity
M	macroscopic quantity
n	time step
p	prescribed degree of freedom

Abbreviations

CH	Computational Homogenization
DNS	Direct Numerical Simulation
FEM	Finite Element Method
LRAM	Locally Resonant Acoustic Metamaterial
RMS	Root Mean Square

Chapter 1

Introduction

Metamaterials are becoming more popular due to their interesting mechanical properties and potential applications. Metamaterials are artificially designed to gain these properties from e.g. their microstructure. These properties are for instance negative Poisson ratio [1], negative dynamic mass density [2], tunable band gaps [3] etc.

An application of metamaterials can be, for instance, the damping of seismic waves [4]. Cubic arrays of iron spheres are connected to a concrete bulk with iron or rubber ligaments such that each sphere can move independently within a surrounding air cavity. This metamaterial can be used as a seismic shield placed around (or underneath) foundations of large civil infrastructure.

Metamaterials gain their unique properties from the underlying microstructure. Therefore, it is desired to accurately model the microstructure in detail. However, the accurate modelling of the microstructure is computationally expensive for large problems. Computational homogenization can be used in these problems. The key feature of the computational homogenization framework is the generality and accuracy compared with other frameworks, while still being computational efficient. In previous work [5, 6], a general computational homogenization framework is developed for a numerical study of the behavior of acoustic metamaterials with nonlinear locally resonant material behavior. A special type of metamaterial is considered, the so-called Locally Resonant Acoustic Metamaterials (LRAMs). In Figure 1.1, a general LRAM configuration is shown. In this work, a simplified 1D version of a locally resonant acoustic metamaterial designed by Liu [7] is used. In these LRAMs, the heavy (red) inclusions are free to move independently inside the matrix (green) due to the soft-coated layer (grey). When a wave with a frequency corresponding to the eigenfrequency of the inclusions enters the material, the heavy inclusions start to resonate. During this process the wave is attenuated. Frequency ranges where this phenomenal occurs are called ‘stop bands’ or ‘band gaps’. In LRAMs these bands are typically in the low-frequency zone.

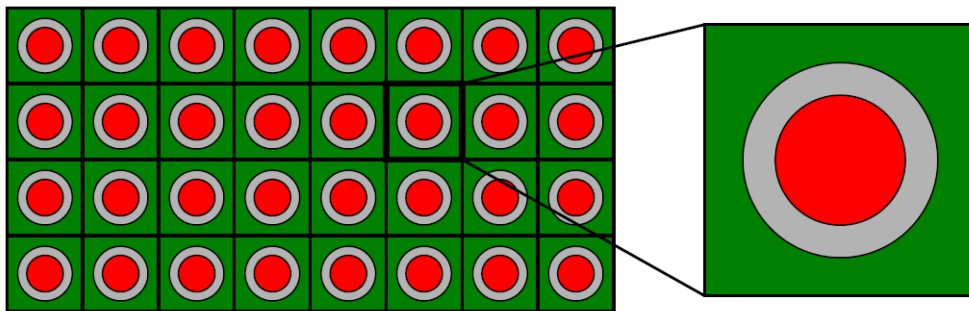


Figure 1.1: An LRAM configuration consisting of a matrix (green) filled with soft-coated (grey) heavy inclusions (red) [5].

In previous work [6], a dynamical computational homogenization framework is presented. This framework is capable of predicting the properties of acoustic metamaterials with non-linear material be-

haviour. The developed model has two positions where the time integration scheme is incorporated, in the microscale and the macroscale. Currently, in both cases, the Newmark scheme [8] with the same parameters ($\gamma = \frac{1}{2}$ and $\beta = \frac{1}{4}$) is used. These parameters are chosen such that it resembles the trapezoidal rule. Furthermore, it is second order accurate and unconditionally stable.

The model, in combination with the trapezoidal rule, is inaccurate for large spatial discretizations and for large simulation times. For large spatial discretizations, spurious oscillations start to occur. From literature [9, 10], this behaviour is typical for the trapezoidal rule.

1.1 Project aim and goals

The goal of this graduation project is to investigate the influence of the time integration scheme on the numerical accuracy of the computational homogenization framework for the behaviour of locally resonant acoustic metamaterials.

1.2 Structure of this report

Chapter 2 gives insight in the time integration schemes and their implementation. A benchmark problem is solved to get familiar with the schemes and to investigate characteristics of the time integration schemes with a focus on characteristics involving wave propagation in Chapter 3. Chapter 4 describes the numerical model and the computational homogenization framework. The results for a fully spatial resolved simulation are shown and discussed in Chapter 5. The computational homogenization results are shown in Chapter 6. Finally, in Chapter 7, the conclusion and recommendations are given.

Chapter 2

Time integration

Time integration schemes are used to discretize the problem in the time domain. Two types of time integration schemes are often used; implicit and explicit time integration. Implicit schemes use the state of the system at the current time and the new time (after a time step). Explicit schemes use only the current state of the system, resulting in less computations. However, in explicit schemes, the time step is very sensitive resulting in the need for small time steps to ensure stability. Implicit methods are less sensitive for large time steps and can therefore be advantageous for large problems where accuracy is of importance. In this project, only implicit time integration schemes are considered.

To investigate the effect of the time integration scheme, different time integration schemes are compared. In literature, several implicit time integration schemes are available which are more accurate for longer time frames and are more accurate for non-linear problems compared to the standard trapezoidal rule. In this chapter, these time integration schemes are described and compared. Then, the most optimal schemes are selected, which are implemented and evaluated during this project. At the end of this chapter, the basic equation of time integration are discussed and the time integration equations for the chosen schemes are shown.

2.1 Time integration schemes

A literature review of existing implicit time integration schemes is performed and the most suitable to this project are shown in Table 2.1. The schemes can be categorized into 'standard' and 'composite' schemes. In the latter case, the time step Δt is split into multiple sub time steps. In each sub time step, a different implicit scheme can be used which has certain advantages (e.g. a sub step with dissipation and one without dissipation). In Figure 2.1, a schematic representation of the sub steps is shown.

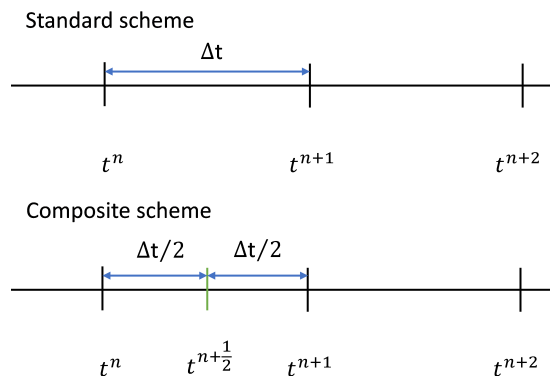


Figure 2.1: Schematic representation of the composite scheme with sub steps.

The time integration scheme used previously in [6]; is second order accurate and unconditionally stable. Therefore, the new time integration scheme needs to possess at least the same properties.

The time integration schemes can possess different properties to adapt to certain conditions (e.g. non-linearity or wave propagation). In order to introduce these properties, some definitions applied to time integration and specifically in wave propagation are discussed:

- Dispersion; Dispersion in wave propagation problems is the phenomena of waves of different wavelengths that travel through a material have different phase speeds. In this work there are two types of dispersion. Numerical dispersion and material dispersion. Numerical dispersion originates from the spatial approximation. Numerical dispersion is the difference in the analytical wave speed versus the approximated (numerical) wave speed in the discretized model [11].
- Dissipation; Dissipation in wave propagation problems is the loss of energy from the wave to the system. In the considered numerical model, no dissipating effects are modelled to keep the model as simple as possible to better understand the influence of time integration schemes. Therefore, dissipation is undesired. However, in the numerical model, high-frequency components that are artifacts from the spatial discretization are present. These components are not representative of the problem to be investigated and therefore it can be advantageous to introduce so-called algorithmic numerical damping of high-frequency components [12]. Non-dissipative time integration schemes do not have this numerical damping property, resulting in energy conservation (see e.g. [12]).

The current time integration scheme, the trapezoidal rule, lacks the dissipation property which causes high frequency spurious modes in the results. Some of the time integration schemes possess the so-called ‘L-stable’ property, which is a special case in the stability region. This property acts as a numerical low-pass filter that suppresses high frequencies and leaves the low frequencies intact.

The implicit time integration schemes that are considered in this project are shown in Table 2.1.

Table 2.1: Standard and composite implicit time integration schemes.

Standard schemes	Composite schemes
Newmark [8]	Bathe β_1/β_2 scheme [9]
trapezoidal scheme (special case of Newmark scheme) [13]	Bathe ρ_∞ scheme [14]
Euler backward scheme [15]	TTBDF scheme (3-substep) [16, 17]
Generalized α -method (Hulbert) [18]	Wen scheme [10]
Backward difference formula [19]	Li scheme (2-substep) [20]
Three-points backward difference formula [21]	Li scheme (3-substep) [22]
Houbolt method [23]	Kim scheme [24]

The Newmark scheme is a well-known time integration scheme. This scheme is dissipative and first order accurate when the parameter $\beta \neq 0.5$. In the special case of $\beta = 0.5$, the scheme becomes the trapezoidal rule, which is second order accurate and non-dissipative [12]. Due to the lack of (numerical) dissipation in the trapezoidal rule, the scheme becomes less accurate in nonlinear dynamics and for long calculation times.

The other standard schemes are all dissipative implicit integration schemes. The disadvantage of dissipative schemes is that they are sensitive for overshooting. In Table 2.2, the properties of the standard schemes are shown.

Table 2.2: Properties of standard implicit time integration schemes

Integration scheme	Accuracy	Stability
Newmark	First order	Conditionally stable
Trapezoidal rule	Second order	Unconditionally stable
Backward Euler	First order	L-stable
Generalized α -method	Second order	Unconditionally stable
Backward Difference Formula	Second order [25]	Conditionally stable
Three-point BDF	Second order	Conditionally stable
Houbolt	Second order [26]	Conditionally stable

The composite schemes are created from the idea of combining standard schemes such that dissipation can be controlled and adapted to special cases, such as nonlinear dynamics or wave propagation. The first composite schemes which uses this idea is the scheme developed by Bathe et al. [9]. This scheme combines the non-dissipative trapezoidal rule with the dissipative backward Euler scheme to control the dissipation and obtain an accurate result in the nonlinear domain. This scheme contains two sub steps. The first sub step is the trapezoidal rule and the second sub step is the backward Euler scheme. This scheme is superior to the trapezoidal rule as analyzed in [22]. Bathe and coworkers expanded this scheme to the Bathe β_1/β_2 [27] scheme and the Bathe ρ_∞ scheme [14]. The original scheme and the Bathe β_1/β_2 scheme are a special case in the Bathe ρ_∞ scheme. For wave propagation problems, Kwon et al [11] recommends certain algorithmic parameters for the Bathe scheme (see Section 2.2.2 for details) which results that the different Bathe schemes are equal. Therefore, the standard Bathe scheme is considered since it is the most simple one with only one algorithmic parameter.

The TTBDF scheme, developed by Chandra et al. [17], is similar to the Bathe scheme since it is also a composite scheme. In this scheme, 3-sub steps are taken. The first and second sub steps are the trapezoidal rule, and the last sub step is the Backward Difference Formula, hence its name (TTBDF). This method possesses numerical dissipation, while maintaining accuracy. The main advantage of this scheme is noticeable in the large deformation, large displacements and large rotation regime. In this regime, it proves more accurate than the Bathe scheme. However, in the other regimes, the schemes are almost equivalent [16]. In these cases, a composite scheme with fewer time steps is preferred because these are computationally more efficient.

Wen et al. [10] developed a composite time integration scheme with three sub steps. In the first sub step, the trapezoidal scheme is considered. The Euler backward scheme is applied in the second sub step and the Houbolt method is used for the last sub step. The advantage of this scheme is the highly controllable numerical dissipation. In this scheme there is only one parameter that can be adjusted. The parameter $w = \frac{1}{3}$ is suggested as desirable for optimal accuracy and numerical dissipation for general non-linear problems [10].

Li et al. [20] proposed a time integration scheme with two sub steps. In the first sub step the first-order backward differential formula is used and for the second sub step the similar three-points backward differential formula with different coefficients is used. In this scheme one parameter can be chosen. It is preferred to chose this parameter in such a way that the scheme is second order accurate. This scheme is unconditionally stable and the accuracy is equal to the Bathe scheme. The advantage over the Bathe scheme is that this scheme requires less matrix-vector operations and is therefore more computational efficient. This scheme is expanded by Li and coworkers in [22] where a new parameter is introduced which can specifically eliminate spurious modes. However, the spurious modes must be known beforehand, which is not the case in this work.

Li and coworkers also proposed a three sub step composite scheme [28]. This scheme is very similar to the previous scheme. However, in some cases, it has less period elongation errors and is more computational efficient.

Kim et al. [24] developed a two sub step time integration scheme where the acceleration from previous time steps is not needed. This results in a higher computational efficiency since the factorization of the mass matrix is unnecessary. The scheme is similar to the Bathe scheme in terms of accuracy and stability. This scheme shows interesting properties since the initial acceleration calculation is currently computationally very costly.

An in-depth comparison is performed in [16] between the Bathe, TTBDf and the Wen scheme. In this paper, certain linear, non-linear and wave propagation benchmark problems are used to compare the three schemes. In case of general linear dynamics, TTBDf>Bathe>Wen is recommended. For wave propagations and cases where numerical dissipation is important, Wen>Bathe>TTBDf is recommended. For general non-linear problems, TTBDf>Wen>Bathe is recommended. However, the Bathe scheme is widely used and implemented in certain software packages and can therefore be more favorable.

In the table below, an overview of the properties of the discussed composite schemes are presented.

Table 2.3: Properties of composite implicit time integration schemes.

Integration scheme	Sub steps	Accuracy	Stability
Bathe β_1/β_2	Trap. rule & Backward Euler	Second order	L-stable
Bathe ρ_∞	Trap. rule & Combination ¹	Second order	Unconditionally stable
TTBDf	Trap. rule & Trap.rule & BDF	Second order	L-stable
Wen	Trap. rule & Backward Euler & Houbolt	Second order	Unconditionally stable
Li (2-substep)	BDF & Three-point BDF	Second order	Unconditionally stable
Li (3-substep)	Backward Euler & BDF & BDF	Second order	L-stable
Kim	Combination & Combination	Second order	L-stable

2.1.1 Integration scheme selection

In the previous section, several implicit time integration schemes are described. Based on the advantages of these schemes and comparison studies, four schemes will be implemented in the developed model. These are the following:

- Bathe standard scheme;
- Wen scheme;
- Li scheme (3 sub steps);
- Kim scheme.

The Bathe standard scheme is chosen because it is widely used, widely studied and implemented in several software packages [16]. The scheme itself is more accurate for nonlinear dynamics and long time frames than the trapezoidal rule.

The Wen scheme looks promising for wave propagation and it will therefore be used in this project. The other advantage of this scheme is that the numerical dispersion and dissipation can be controlled extensively.

The Li three sub step scheme is chosen because it is computationally efficient without losing accuracy. However, the accuracy remains questionable in the LRAM specific case.

The Kim scheme is chosen because the acceleration from previous steps is not needed in the calculation. In the current model, the prediction of the acceleration is computational costly and this scheme can therefore be very efficient.

¹Depending on parameter, one of the standard schemes can be found

2.2 The basic equations of time integration

The governing equation that needs to be solved is:

$$\mathbf{M}\ddot{\mathbf{u}} + \mathbf{F}(\mathbf{u}, t) = \mathbf{R}(t). \quad (2.1)$$

Here, \mathbf{M} is the mass matrix, \mathbf{u} is the vector of nodal displacements, \mathbf{F} is the vector of nodal internal point force, \mathbf{R} is the external forces on the system and an overdot indicates the time derivative. Another form of this equation is expressed as:

$$\mathbf{M}\ddot{\mathbf{u}} + \mathbf{K}\mathbf{u} = \mathbf{R}(t), \quad (2.2)$$

where \mathbf{K} is the (tangent) stiffness matrix. To solve this equation numerically, the equation is discretized with time steps Δt . In each time step the equation is solved. Table 2.4 and 2.5 show a step-by-step solution for the trapezoidal rule and for the composite scheme (in the table, the Bathe scheme is used as example), respectively. For non-linear problems, the same step-by-step solution can be used with an iterative scheme (e.g. Newton-Rhaphson) as addition. With the use of an iterative scheme, after each time step and/or sub step, the new displacements are guessed by assuming the new accelerations as zero. At the end of the time step and/or sub step, convergence is checked. When the convergence check fails, the displacements are updated and the same steps are repeated until convergence. If convergence is reached, the velocities and accelerations are updated, and the next time step and/or sub step is started.

Table 2.4: Step-by-step solution for the trap integration scheme. Adapted from [29].

- A. Initial calculations:
 1. Initialize stiffness matrix \mathbf{K} and mass matrix \mathbf{M} .
 2. Initialize \mathbf{u}^0 , $\dot{\mathbf{u}}^0$ and $\ddot{\mathbf{u}}^0$.
 3. Select time step Δt .
 4. Calculate effective stiffness matrix $\hat{\mathbf{K}}$:

$$\hat{\mathbf{K}} = \mathbf{K} + \frac{4}{\Delta t^2}\mathbf{M};$$
- B. For each time step:
 1. Guess displacements at time $t + \Delta t$:

$$\mathbf{u}^{t+\Delta t} = \mathbf{u}^t + \Delta t\dot{\mathbf{u}}^t + \frac{(\Delta t)^2}{2}\ddot{\mathbf{u}}^t.$$
 2. Calculate effective loads at time $t + \Delta t$:

$$\hat{\mathbf{R}}^{t+\Delta t} = \mathbf{R}^{t+\Delta t} + \mathbf{M}\left(\frac{4}{\Delta t^2}(\mathbf{u}^{t+\Delta t} - \mathbf{u}^t) - \frac{4}{\Delta t}\dot{\mathbf{u}}^t - \ddot{\mathbf{u}}^t\right).$$
 3. Solve for displacements:

$$\hat{\mathbf{K}}\mathbf{u}^{t+\Delta t} = \hat{\mathbf{R}}^{t+\Delta t}.$$
 4. Calculate velocities and accelerations at time $t + \Delta t$:

$$\ddot{\mathbf{u}}^{t+\Delta t} = \frac{4}{\Delta t^2}(\mathbf{u}^{t+\Delta t} - \mathbf{u}^t) - \frac{4}{\Delta t}\dot{\mathbf{u}}^t - \ddot{\mathbf{u}}^t;$$

$$\dot{\mathbf{u}}^{t+\Delta t} = \dot{\mathbf{u}}^t + \frac{\Delta t}{2}(\ddot{\mathbf{u}}^t + \ddot{\mathbf{u}}^{t+\Delta t}).$$

Table 2.5: Step-by-step solution for the Bathe integration scheme. Other composite scheme step-by-step solutions have a similar solution strategy. Only the displacement, velocity and acceleration calculations and the integration constant are different. Adapted from [29].

- A. Initial calculations:
1. Initialize stiffness matrix \mathbf{K} and mass matrix \mathbf{M} .
 2. Initialize \mathbf{u}^0 , $\dot{\mathbf{u}}^0$ and $\ddot{\mathbf{u}}^0$.
 3. Select time step Δt and select integration constants (c_1, c_2, c_3) .
 4. Calculate effective stiffness matrix $\hat{\mathbf{K}}_1$ and $\hat{\mathbf{K}}_2$:

$$\hat{\mathbf{K}}_1 = \mathbf{K} + \frac{4}{(b\Delta t)^2}\mathbf{M}; \quad \hat{\mathbf{K}}_2 = \mathbf{K} + c_3^2\mathbf{M}.$$
- B. For each time step:
- First sub step:
1. Guess displacement at time step $t + b\Delta t$:

$$\mathbf{u}^{t+b\Delta t} = \mathbf{u}^t + \frac{b\Delta t}{2}\dot{\mathbf{u}}^t + \frac{(b\Delta t)^2}{4}\ddot{\mathbf{u}}^t.$$
 2. Calculate effective loads at time $t + b\Delta t$:

$$\hat{\mathbf{R}}^{t+b\Delta t} = \mathbf{R}^{t+b\Delta t} + \mathbf{M}\left(\frac{4}{(b\Delta t)^2}\mathbf{u}^{t+b\Delta t} + \frac{4}{b\Delta t}\dot{\mathbf{u}}^t + \ddot{\mathbf{u}}^t\right).$$
 3. Solve for displacements:

$$\hat{\mathbf{K}}_1\mathbf{u}^{t+b\Delta t} = \hat{\mathbf{R}}^{t+b\Delta t}.$$
 4. Calculate velocities and accelerations at time $t + b\Delta t$:

$$\dot{\mathbf{u}}^{t+b\Delta t} = \frac{2}{b\Delta t}(\mathbf{u}^{t+b\Delta t} - \mathbf{u}^t) - \dot{\mathbf{u}}^t;$$

$$\ddot{\mathbf{u}}^{t+b\Delta t} = \frac{2}{b\Delta t}(\dot{\mathbf{u}}^{t+b\Delta t} - \dot{\mathbf{u}}^t) - \ddot{\mathbf{u}}^t.$$
- Second sub step:
1. Guess displacement at time $t + \Delta t$:

$$\mathbf{u}^{t+\Delta t} = -\frac{c_1}{c_3}\mathbf{u}^t - \frac{c_2}{c_3}\mathbf{u}^{t+b\Delta t} - \frac{c_1}{c_3^2}\dot{\mathbf{u}}^t - \frac{c_2}{c_3^2}\dot{\mathbf{u}}^{t+b\Delta t}.$$
 1. Calculate effective loads at time $t + \Delta t$:

$$\hat{\mathbf{R}}^{t+\Delta t} = \mathbf{R}^{t+\Delta t} + \mathbf{M}(-c_2c_3\mathbf{u}^{t+b\Delta t} - c_1c_3\mathbf{u}^t - c_2\dot{\mathbf{u}}^{t+b\Delta t} - c_1\dot{\mathbf{u}}^t).$$
 2. Solve for displacements:

$$\hat{\mathbf{K}}_2\mathbf{u}^{t+\Delta t} = \hat{\mathbf{R}}^{t+\Delta t}.$$
 3. Calculate velocities and accelerations at time $t + \Delta t$:

$$\dot{\mathbf{u}}^{t+\Delta t} = c_1\dot{\mathbf{u}}^t + c_2\dot{\mathbf{u}}^{t+b\Delta t} + c_3\dot{\mathbf{u}}^{t+\Delta t};$$

$$\ddot{\mathbf{u}}^{t+\Delta t} = c_1\ddot{\mathbf{u}}^t + c_2\ddot{\mathbf{u}}^{t+b\Delta t} + c_3\ddot{\mathbf{u}}^{t+\Delta t}.$$

2.2.1 Trapezoidal rule

The trapezoidal rule determines the unknown displacements $\mathbf{u}^{t+\Delta t}$ and velocities $\dot{\mathbf{u}}^{t+\Delta t}$ at the next time step $t + \Delta t$ as:

$$\mathbf{u}^{t+\Delta t} = \mathbf{u}^t + \Delta t\dot{\mathbf{u}}^t + \left(\frac{1}{2} - \beta\right)\Delta t^2\ddot{\mathbf{u}}^t + \beta\Delta t^2\ddot{\mathbf{u}}^{t+\Delta t}, \quad (2.3)$$

$$\dot{\mathbf{u}}^{t+\Delta t} = \dot{\mathbf{u}}^t + (1 - \gamma)\Delta t\ddot{\mathbf{u}}^t + \gamma\Delta t\ddot{\mathbf{u}}^{t+\Delta t}. \quad (2.4)$$

Here, Δt is a fixed time step, β and γ are the Newmark constants controlling the integration scheme. The new displacements and velocities depend on the known state of the system at the current time step t and on the unknown acceleration $\ddot{\mathbf{u}}^{t+\Delta t}$ at the next time step. The new displacements and velocities are predicted by assuming $\ddot{\mathbf{u}}^{t+\Delta t} = 0$ and correcting for this assumption with the calculated predicted new displacements and velocities.

2.2.2 Bathe scheme

In the Bathe scheme b is the algorithmic parameter controlling the scheme. After the displacement is guessed, calculate velocities and accelerations at time step $t + b\Delta t$:

$$\dot{\mathbf{u}}^{t+b\Delta t} = \frac{2}{b\Delta t}\mathbf{u}^{t+b\Delta t} - \frac{2}{b\Delta t}\mathbf{u}^t - \dot{\mathbf{u}}^t, \quad (2.5)$$

$$\ddot{\mathbf{u}}^{t+b\Delta t} = \frac{2}{b\Delta t}\dot{\mathbf{u}}^{t+b\Delta t} - \frac{2}{b\Delta t}\dot{\mathbf{u}}^t - \ddot{\mathbf{u}}^t. \quad (2.6)$$

Second sub step, the velocities and accelerations at time step $t + \Delta t$ are calculated via:

$$\dot{\mathbf{u}}^{t+\Delta t} = c_1\dot{\mathbf{u}}^t + c_2\dot{\mathbf{u}}^{t+b\Delta t} + c_3\dot{\mathbf{u}}^{t+\Delta t}, \quad (2.7)$$

$$\ddot{\mathbf{u}}^{t+\Delta t} = c_1\ddot{\mathbf{u}}^t + c_2\ddot{\mathbf{u}}^{t+b\Delta t} + c_3\ddot{\mathbf{u}}^{t+\Delta t}, \quad (2.8)$$

with

$$c_1 = \frac{1-b}{b\Delta t}, \quad c_2 = \frac{-1}{(1-b)b\Delta t}, \quad c_3 = \frac{2-b}{(1-b)\Delta t}. \quad (2.9)$$

In the initial implementation of the Bathe scheme, the parameter b is defined as 0.5. In general cases for linear and nonlinear problems this value results in accurate solutions [27].

2.2.3 Wen scheme

In the first sub step, the new displacements and velocities at time step $t + w\Delta t$ are:

$$\dot{\mathbf{u}}^{t+w\Delta t} = \dot{\mathbf{u}}^t + \frac{1}{2}w\Delta t(\ddot{\mathbf{u}}^t + \ddot{\mathbf{u}}^{t+w\Delta t}), \quad (2.10)$$

$$\mathbf{u}^{t+w\Delta t} = \mathbf{u}^t + \frac{1}{2}w\Delta t(\dot{\mathbf{u}}^t + \dot{\mathbf{u}}^{t+b\Delta t}), \quad (2.11)$$

where w is the parameter controlling the integration scheme. The same procedure is followed where the new accelerations are assumed to be zero and after the calculation of the new displacements and velocities, the accelerations are updated. In the second sub step, $t + (1-w)\Delta t$, the new displacements and velocities are calculated via:

$$\mathbf{u}^{t+(1-w)\Delta t} = \frac{c_2}{c_3}\mathbf{u}^{t+w\Delta t} - \frac{c_1}{c_3}\mathbf{u}^t + \frac{c_2\Delta t}{c_3^2}\dot{\mathbf{u}}^{t+w\Delta t} - \frac{c_1\Delta t}{c_3^2}\dot{\mathbf{u}}^t + \frac{\Delta t^2}{c_3^2}\ddot{\mathbf{u}}^{t+(1-w)\Delta t}, \quad (2.12)$$

$$\dot{\mathbf{u}}^{t+(1-w)\Delta t} = \frac{c_2}{c_3}\dot{\mathbf{u}}^{t+w\Delta t} - \frac{c_1}{c_3}\dot{\mathbf{u}}^t + \frac{\Delta t}{c_3}\ddot{\mathbf{u}}^{t+(1-w)\Delta t}, \quad (2.13)$$

where the parameters c_1 , c_2 and c_3 are defined as:

$$c_1 = \frac{2w-1}{w(w-1)}, \quad c_2 = \frac{1-w}{w(2w-1)}, \quad c_3 = \frac{2-3w}{(w-1)(2w-1)}. \quad (2.14)$$

The new displacements and velocities in the last sub step $t + \Delta t$ are given as:

$$\begin{aligned} \mathbf{u}^{t+\Delta t} = & -\frac{d_1}{d_4}\mathbf{u}^t - \frac{d_2}{d_4}\mathbf{u}^{t+w\Delta t} - \frac{d_3}{d_4}\mathbf{u}^{t+(1-w)\Delta t} - \frac{\Delta t d_1}{d_4^2}\dot{\mathbf{u}}^t - \frac{\Delta t d_2}{d_4^2}\dot{\mathbf{u}}^{t+w\Delta t} \\ & - \frac{\Delta t d_3}{d_4^2}\dot{\mathbf{u}}^{t+(1-w)\Delta t} + \frac{\Delta t^2}{d_4^2}\ddot{\mathbf{u}}^{t+\Delta t}, \end{aligned} \quad (2.15)$$

$$\dot{\mathbf{u}}^{t+\Delta t} = -\frac{d_1}{d_4}\dot{\mathbf{u}}^t - \frac{d_2}{d_4}\dot{\mathbf{u}}^{t+w\Delta t} - \frac{d_3}{d_4}\dot{\mathbf{u}}^{t+(1-w)\Delta t} + \frac{\Delta t}{d_4}\ddot{\mathbf{u}}^{t+\Delta t}. \quad (2.16)$$

The parameters d_1 , d_2 , d_3 and d_4 are defined as:

$$d_1 = -1, \quad d_2 = \frac{1}{(w-1)(2w-1)}, \quad d_3 = \frac{1}{w(2w-1)}, \quad d_4 = \frac{w^2-w-1}{w(w-1)}. \quad (2.17)$$

The parameter w is initially chosen as $\frac{1}{3}$ since this results in a general accurate solution [10].

2.2.4 Kim scheme

In the first sub step the displacements and velocities are given by:

$$\mathbf{u}^{t+\tau\Delta t} = \mathbf{u}^t + \tau\Delta t\dot{\mathbf{u}}^{t+\tau\Delta t}, \quad (2.18)$$

$$\dot{\mathbf{u}}^{t+\tau\Delta t} = \dot{\mathbf{u}}^t + \tau\Delta t\ddot{\mathbf{u}}^{t+\tau\Delta t}. \quad (2.19)$$

In these equations, τ is the algorithmic parameter controlling the scheme. In the second time step the displacements and velocities are determined via:

$$\mathbf{u}^{t+\Delta t} = \mathbf{u}^t + \Delta t \left((1 - \alpha)\dot{\mathbf{u}}^{t+\tau\Delta t} + \alpha\dot{\mathbf{u}}^{t+\Delta t} \right), \quad (2.20)$$

$$\dot{\mathbf{u}}^{t+\Delta t} = \dot{\mathbf{u}}^t + \Delta t \left((1 - \alpha)\ddot{\mathbf{u}}^{t+\tau\Delta t} + \alpha\ddot{\mathbf{u}}^{t+\Delta t} \right), \quad (2.21)$$

where α is the algorithmic parameter determining the amount of dissipation in the scheme. Finally, the displacements and velocities at time step $t + \Delta t$ are updated with the calculated accelerations $\dot{\mathbf{u}}^{t+\tau\Delta t}$ and $\ddot{\mathbf{u}}^{t+\Delta t}$ as:

$$\dot{\mathbf{u}}^{t+\Delta t} = \dot{\mathbf{u}}^t + \Delta t \left((1 - \beta)\ddot{\mathbf{u}}^{t+\tau\Delta t} + \beta\ddot{\mathbf{u}}^{t+\Delta t} \right), \quad (2.22)$$

$$\mathbf{u}^{t+\Delta t} = \mathbf{u}^t + \Delta t \left((1 - \beta)\dot{\mathbf{u}}^{t+\tau\Delta t} + \beta\dot{\mathbf{u}}^{t+\Delta t} \right), \quad (2.23)$$

where β is the algorithmic parameter. The Kim scheme is different from the other composite schemes since the update of the final displacements and velocities (after the second sub step) can have a different parameter (β) than the parameter (α) that is used to guess the initial displacements and velocities at the start of the second sub step. Initially, the parameter $\tau = \frac{1}{4}$ is used and α and β are defined as:

$$\alpha = \tau, \quad \beta = \frac{2\tau - 1}{2(\tau - 1)}. \quad (2.24)$$

These values for the parameters results in a optimal scheme for general problems [24].

2.2.5 Li scheme

The Li schemes calculates the displacements and velocities in the first sub step as:

$$\mathbf{u}^{t+\tau\Delta t} = \mathbf{u}^t + \tau\Delta t\dot{\mathbf{u}}^{t+\tau\Delta t}, \quad (2.25)$$

$$\dot{\mathbf{u}}^{t+\tau\Delta t} = \dot{\mathbf{u}}^t + \tau\Delta t\ddot{\mathbf{u}}^{t+\tau\Delta t}. \quad (2.26)$$

In these equations, τ indicates the algorithmic parameter. In the second sub step, the velocities and accelerations are calculated via:

$$\dot{\mathbf{u}}^{t+\Delta t} = \frac{d_0}{\Delta t}\mathbf{u} + \frac{d_1}{\Delta t}\mathbf{u}^{t+\tau\Delta t} + \frac{d_2}{\Delta t}\mathbf{u}^{t+\Delta t}, \quad (2.27)$$

$$\ddot{\mathbf{u}}^{t+\Delta t} = \frac{d_0}{\Delta t}\dot{\mathbf{u}} + \frac{d_1}{\Delta t}\dot{\mathbf{u}}^{t+\tau\Delta t} + \frac{d_2}{\Delta t}\dot{\mathbf{u}}^{t+\Delta t}, \quad (2.28)$$

where d_0 , d_1 and d_2 are:

$$d_0 = \frac{1 - 2\tau}{\tau^2}, \quad d_1 = \frac{\tau - 1}{\tau^2}, \quad d_2 = \frac{1}{\tau}. \quad (2.29)$$

Chapter 3

Benchmark problem

A benchmark problem is conducted on the considered implicit time integration schemes in order to get familiarized with the schemes and verify the implementation. The problem is a 1D mass-spring system with linear springs. The papers where the integration schemes are introduced all have this benchmark problem as a model problem. Hence, the implementation in this project can be easily verified against the results in the papers.

The governing equations for the 3 degree-of-freedom spring system shown in Figure 3.1 are:

$$\begin{bmatrix} m_1 & 0 & 0 \\ 0 & m_2 & 0 \\ 0 & 0 & m_3 \end{bmatrix} \begin{bmatrix} \ddot{u}_1 \\ \ddot{u}_2 \\ \ddot{u}_3 \end{bmatrix} + \begin{bmatrix} k_1 & -k_1 & 0 \\ -k_1 & k_1 + k_2 & -k_2 \\ 0 & -k_2 & k_2 \end{bmatrix} \begin{bmatrix} u_1 \\ u_2 \\ u_3 \end{bmatrix} = \begin{bmatrix} R_1 \\ 0 \\ 0 \end{bmatrix}. \quad (3.1)$$

In this problem, $k_1 = 10^7$, $k_2 = 1$, $m_1 = 0$, $m_2 = m_3 = 1$ and the prescribed displacement on node 1 is $u_1 = \sin(\omega_p t)$ with $\omega_p = 1.2$. Since the displacement is prescribed, the system of equations is rewritten to solve for the unknown displacements u_2 and u_3 :

$$\begin{bmatrix} m_2 & 0 \\ 0 & m_3 \end{bmatrix} \begin{bmatrix} \ddot{u}_2 \\ \ddot{u}_3 \end{bmatrix} + \begin{bmatrix} k_1 + k_2 & -k_2 \\ -k_2 & k_2 \end{bmatrix} \begin{bmatrix} u_2 \\ u_3 \end{bmatrix} = \begin{bmatrix} k_1 u_1 \\ 0 \end{bmatrix}, \quad (3.2)$$

with the reaction obtained as:

$$R_1 = m_1 \ddot{u}_1 + k_1 u_1 - k_1 u_2 \quad (3.3)$$

This benchmark problem is chosen because it represents stiff and flexible parts in a complex structural system. The left spring has a high stiffness while the right spring has a low stiffness to represent a flexible part. Secondly, this model problem is a very simplified version of the LRAM.

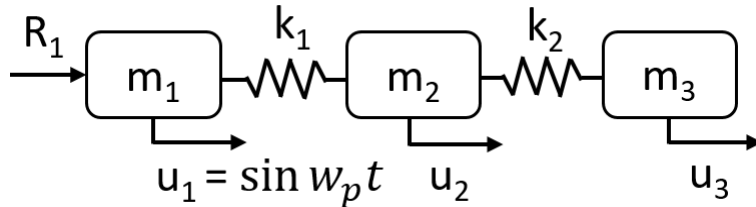


Figure 3.1: Schematic of 1D model problem of three degrees of freedom spring system, $k_1 = 10^7$, $k_2 = 1$, $m_1 = 0$, $m_2 = m_3 = 1$ and $w_p = 1.2$. Inspired from [27].

The system is solved by using initial conditions for the displacements, velocities and acceleration as 0. The analytical solution is calculated via mode superposition. This method calculates the response accurately and discards the dynamic response in the high frequency mode which is created due to modelling. In the solution, the time integration schemes all have a normalized time step, meaning that

a two sub step scheme has a time step that is twice that of a one sub step scheme and a three sub step scheme thrice. This is done in order to accurately compare the schemes by using a similar time (sub) step and now these schemes have a comparable computational cost.

The calculated solution for the displacements of the second node can be seen in Figure 3.2. Figures 3.3-3.6 show the solutions for the velocities, accelerations of node 2 and the displacements, velocities and accelerations of node 3. All schemes except the Li scheme have an accurate solution while the Li scheme overshoots the analytical solution. The Li scheme does not perform well in the velocities and accelerations of node 2. The solution has a very large overshoot (which is also slightly observed in the displacements). However, in the solutions of node 3, this is not observed at all and the solution of node 3 is accurate with respect to the analytical solution and also with respect to the solution provided in [20], where the scheme is first described. Unfortunately, the solution of node 2 is not shown.

A similar observation can be done for the Kim scheme. The solution is accurate and comparable with the analytical solution of node 2 while the solution of node 3 is inaccurate. In [24], this scheme is also applied to the same benchmark problem, however the solution of node 3 is not included.

The trapezoidal rule solution is accurate for the displacements of node 2 & 3 and for the velocities and accelerations of node 3. However, the velocities and accelerations of node 2 are not accurate and high frequency spurious oscillations start to occur. This phenomena is occurring on the stiff node (2) while on the flexible node (3) no spurious oscillations are observed. In Section 2.4, this is further discussed.

Both the Bathe and the Wen scheme solutions are accurate for both nodes. These results show no spurious oscillations or other errors. There is only an undershoot and overshoot for the Bathe and Wen scheme, respectively, at the very first time step, which can be explained analytical [10, 27].

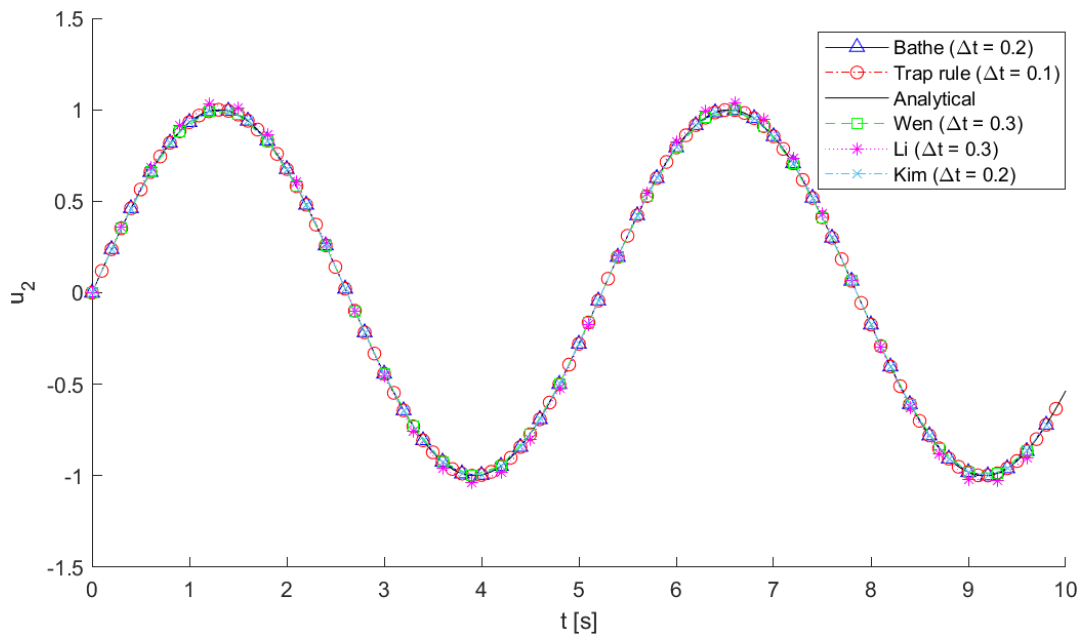


Figure 3.2: Displacements of node 2 for different implicit time integration schemes with corrected time step.

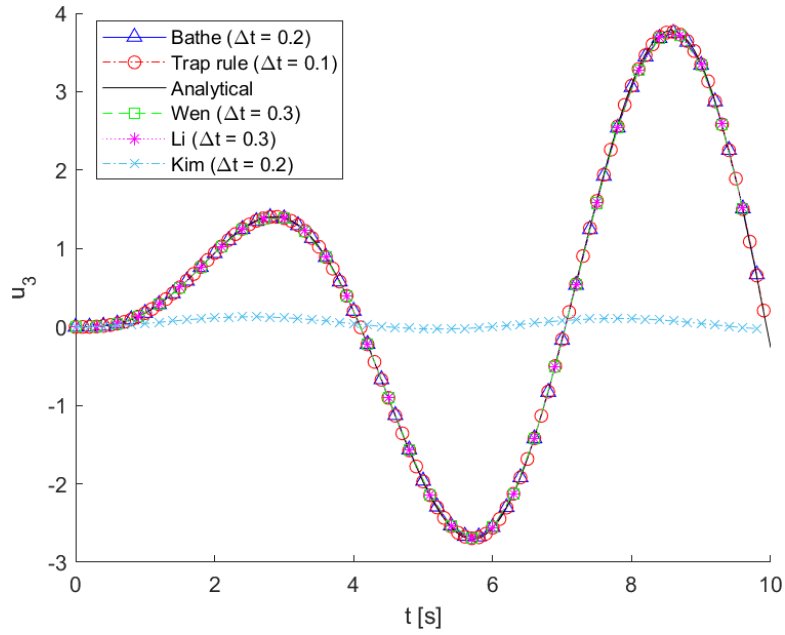


Figure 3.3: Displacements of node 3 for different implicit time integration schemes with corrected time step.

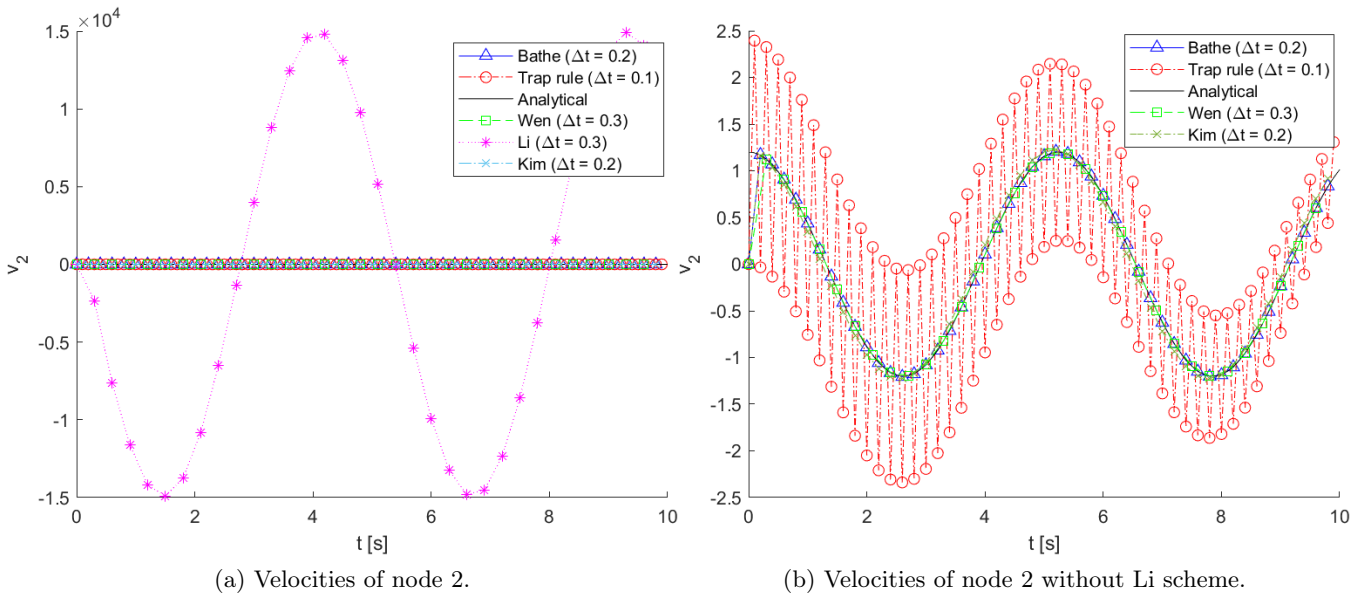


Figure 3.4: Velocities of node 2 for different implicit time integration schemes with corrected time step.

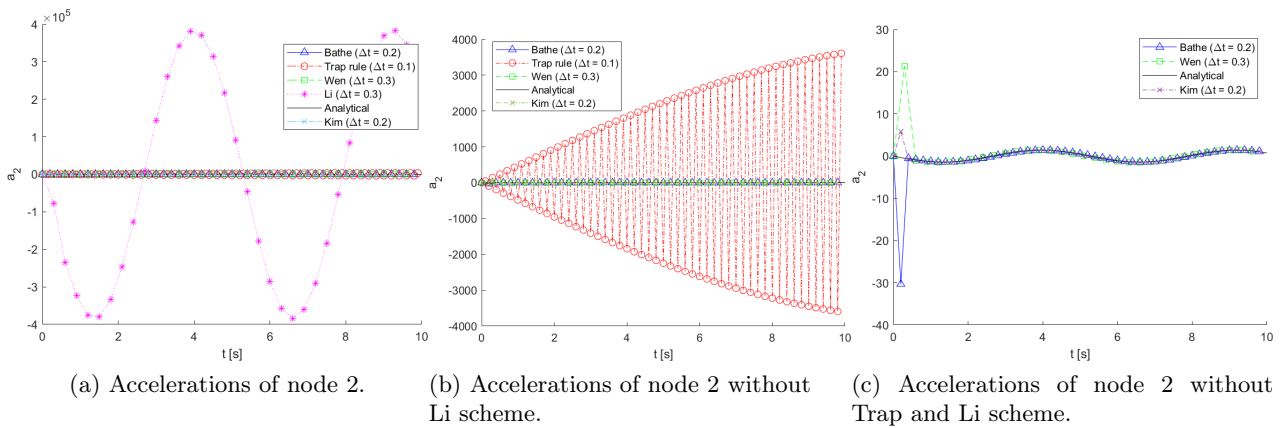


Figure 3.5: Accelerations of node 2 for different implicit time integration schemes with corrected time step.

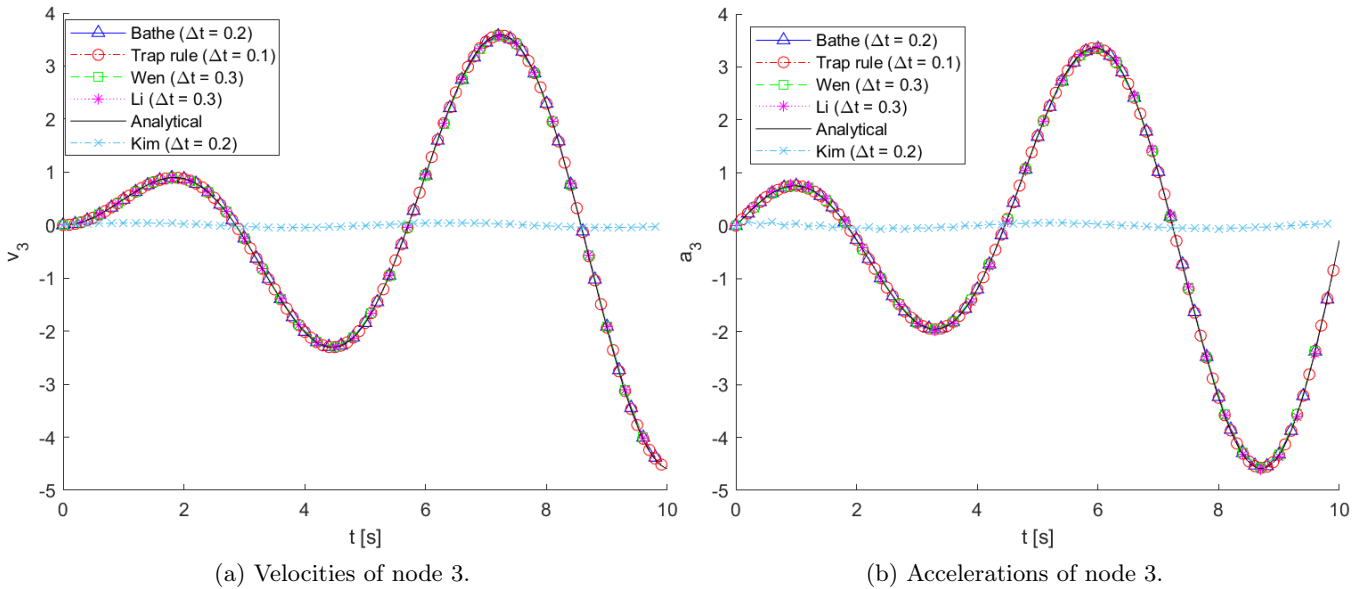


Figure 3.6: Velocities and accelerations of node 3 for different implicit time integration schemes with corrected time step.

3.1 Discussion

The Li and Kim scheme are not further considered in this project since the solution to the benchmark problem are not accurate and the papers introducing the schemes do not cover the respective nodes where the schemes are not accurate (while covering the node with an accurate response). This leaves the current time integration scheme, the trapezoidal rule, and the new schemes, the Bathe and Wen scheme to be considered in this project.

The solution of the trapezoidal rule in the benchmark problem shows high frequency spurious oscillations in the stiff node while the flexible node does not show spurious oscillations. In Section 2.1, the non-dissipative property of the trapezoidal rule is discussed. The stiff node introduces high frequency modes to the system and this non-dissipative property includes the high frequency modes in the solution. Hence, the spurious oscillations in the solution. The benchmark problem is defined in such a way that the importance of high frequency modes is amplified. In Figure 3.7, the velocities

of the same benchmark problem is shown but with a varying stiffness of the stiff node (2) for the trapezoidal rule and the Bathe scheme. For low stiffness, $k_1 = 1 - 10$, the trapezoidal rule is similar to the Bathe scheme. For an intermediate stiffness, $k_1 = 100$, the trapezoidal rule and the Bathe scheme are accurate for low simulation times but in the high simulation times the trapezoidal rule starts to diverge from the Bathe scheme. A stiffness of $k_1 = 1000$ results in these spurious oscillations for the trapezoidal rule while the Bathe scheme only shows this in the earlier time steps.

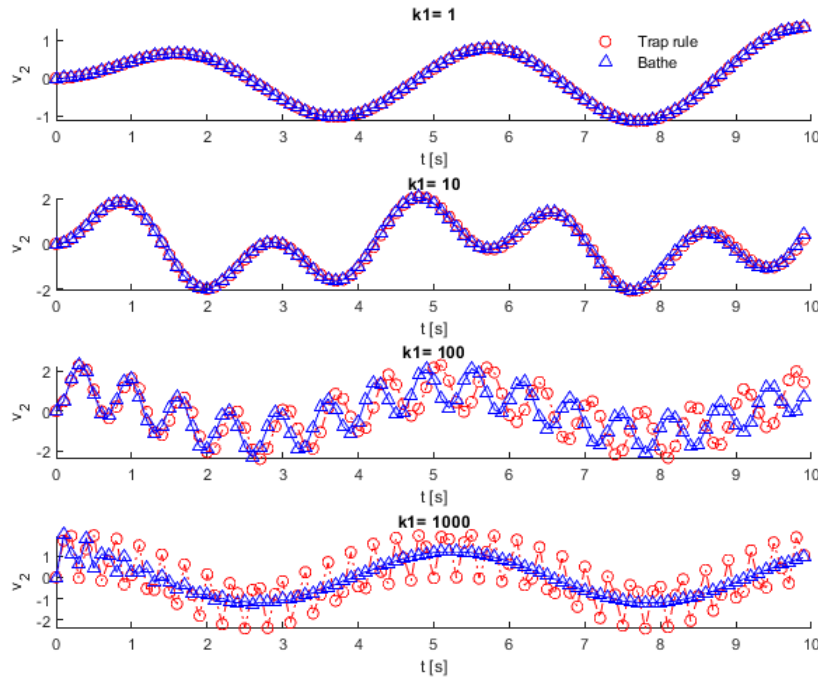


Figure 3.7: Velocity of node 2 with varying stiffness of spring k_1 in benchmark problem (Figure 3.1) for the trapezoidal rule and the Bathe scheme, both with $\Delta t = 0.1$.

Figure 3.8 shows the absolute error of the displacement of node 2 for the trapezoidal rule, Bathe and Wen scheme with their corrected time step. The trapezoidal rule has the least amount of error when the time steps are corrected. However, the trapezoidal rule does have spurious high frequencies oscillations in the velocity and acceleration. Since the relative computational cost is not relevant when the scheme is not accurate (the trapezoidal rule solution for the velocities and acceleration), the same time step is used for all three schemes. This is shown in Figure 3.9. Now, the trapezoidal rule is the least accurate.

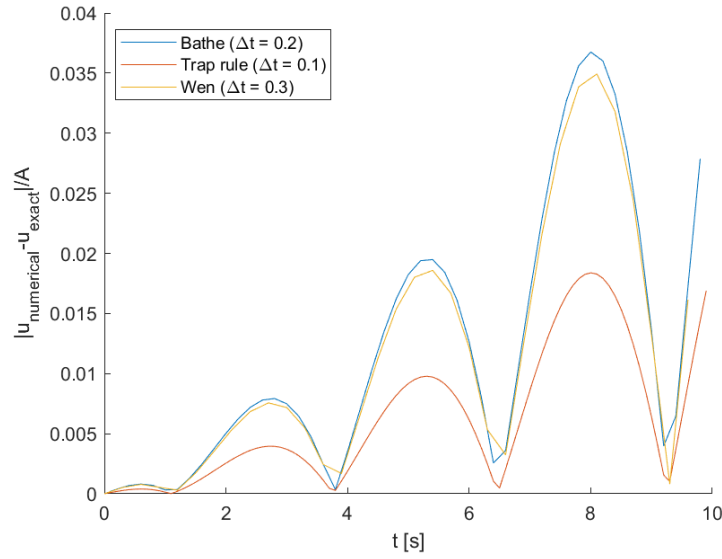


Figure 3.8: Absolute error of the displacement of node 2 w.r.t. the analytical solution. The integration schemes have their corrected time steps.

The second order accuracy of the three schemes is studied. In Chapter 2.1, it is discussed that all three schemes are second order accurate. To study this, time step is varied and the absolute error of the displacement of node 2 versus the analytical error is calculated. In Figure 3.10 this is shown. The figure shows that the error is smaller when a smaller time step is used and this relation has a slope of 2, proving the second order accuracy.

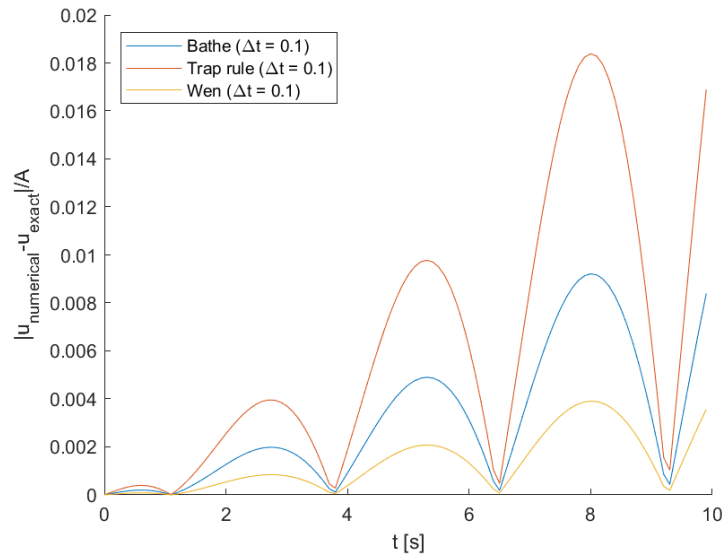


Figure 3.9: Absolute error of the displacement of node 2 w.r.t. the analytical solution. The integration schemes have the same time steps.

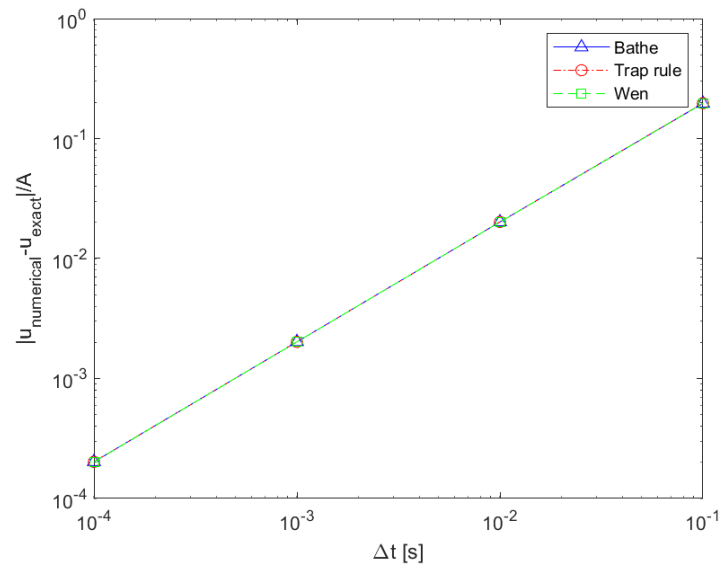


Figure 3.10: Convergence rates of the trapezoidal, Bathe and Wen scheme.

Chapter 4

Numerical model

In Chapter 3, the benchmark problem is solved in a discrete manner. The characteristics of the time integration schemes are discussed for this case. This chapter describes the simulation setup of the locally resonant acoustic metamaterial, where time and space are discretized. The discretization of the model in space and the consequential characteristics of the time integration schemes are described in the following sections. It also describes the computational homogenization framework.

4.1 Direct numerical simulation

Direct Numerical Simulation (DNS) is a method to solve a system by fully describing the system in the space and time domain. The DNS simulations consists of unit cells which are connected to each other. Therefore, the DNS simulations are fully spatially resolved. Simulations are performed on a 1D version of a locally resonant acoustic metamaterial designed by Liu [7]. Therefore, 2D and 3D wave interactions are not taken into account.

Liu’s design of a locally resonant acoustic metamaterial can be seen in Figure 4.1. The LRAM consists of three materials: an epoxy matrix (green), silicone rubber (gray) and a lead core (red). The rubber ensures that the lead core can move independently from the matrix material, resulting in the source of the locally resonant modes.

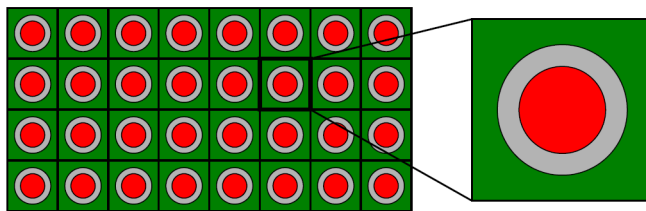


Figure 4.1: A general LRAM configuration consisting of a matrix (green) filled with soft-coated (grey) heavy inclusions (red). Reprinted from [5].

The 1D simplified version of the LRAM considered in this work can be seen in Figure 4.2. The associated geometrical and material properties are shown in Table 4.1.

In this work, the Finite Element Method (FEM) is used for the simulations. In appendix A, the main

Table 4.1: Geometric and material properties of the unit cell in Figure 4.2 [6].

Geometric properties	Value [mm]	Material properties	Epoxy	Rubber	Lead
Length of RVE	l_m 25.2	Density	ρ , kg/m ³ 1.18×10^3	1.30×10^3	1.16×10^4
Thickness of rubber coating	t_c 2.5	Young’s modulus	E , N/m ² 4.35×10^9	1.18×10^5	4.05×10^{10}
Diameter of the lead core	d 10.0				

derivations can be found. The unit cell is discretized into 55 elements. The rubber material has the

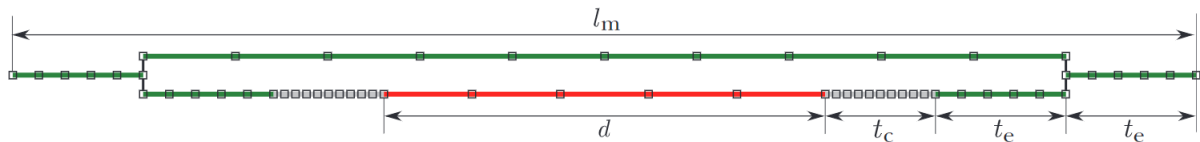


Figure 4.2: Numerical 1D model of Liu's LRAM model with Finite Element discretization. Consists of three materials: Epoxy matrix (green), silicone rubber coating (gray) and lead core (red) [6].

smallest element size since the largest strains are expected in this material.

The dispersion spectrum of the RVE is analysed in previous work [5]. The dispersion spectrum shows the wavenumber for different frequencies. The wavenumber is expressed as $k = \omega/c$ where ω is the frequency and c the velocity of the wave. Positive wavenumbers k denote propagating waves and negative wavenumbers k indicate evanescent waves. Evanescent waves are reflected waves resulting from the locally resonant material, which result in the overall attenuation of the wave. The dispersion spectrum can be seen in Figure 4.3. The band gap of the metamaterial is approximately between 140 Hz and 310 Hz. The band gap is associated with the eigenfrequency of the rubber coated lead core, which is 142 Hz. In the figure, it can be observed that there are no propagative dispersion branches in this region corresponding to other eigenmodes.

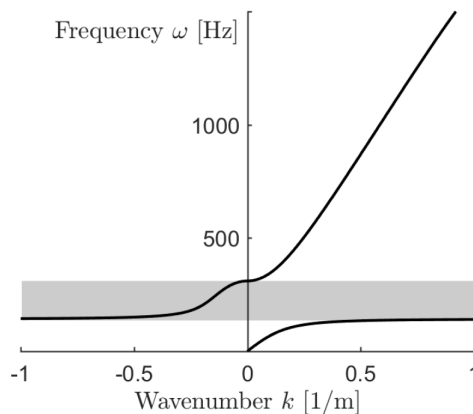


Figure 4.3: Dispersion spectrum and band gap (gray area) of the unit cell. Positive wavenumbers k denote propagating waves. Negative wavenumbers k denote evanescent waves. Reprinted from [5].

Boundary conditions are necessary to solve the system. In this project, the boundary conditions are applied by means of prescribed displacement. The simulations are performed in one dimension without any numerical damping. In previous work [5, 6], numerical damping in the form of Rayleigh damping was added to the system for numerical stability. The (numerical) damping in the current system results purely from the time integration schemes (as discussed in Chapter 2).

The boundary conditions are as follows: the end of the system (at the last unit cell) is fixed and at the start of the system (the first unit cell), a periodic excitation is applied with an amplitude A and frequency ω for the entire simulation duration as:

$$u^{(0)} = A \sin(2\pi\omega t), \quad u^{l_M} = 0. \quad (4.1)$$

The displacement of the two prescribed nodes is known at all times t , the velocity and acceleration of the prescribed nodes can be derived as:

$$\dot{u}^{(0)} = 2\pi\omega A \cos(2\pi\omega t), \quad \dot{u}^{l_M} = 0, \quad (4.2)$$

$$\ddot{u}^{(0)} = -(2\pi\omega)^2 A \sin(2\pi\omega t), \quad \ddot{u}^{l_M} = 0. \quad (4.3)$$

The initial displacement, velocity and acceleration of all the nodes are required for the time integration schemes. The system starts from rest, meaning that the initial displacement, velocity and acceleration of the free nodes (denoted by f) are defined as:

$$\mathbf{u}^{(f)} = \mathbf{0}, \quad (4.4)$$

$$\dot{\mathbf{u}}^{(f)} = \mathbf{0}, \quad (4.5)$$

$$\ddot{\mathbf{u}}^{(f)} = \mathbf{0}. \quad (4.6)$$

4.2 Computational homogenization simulations

In this section, the Computational Homogenization (CH) framework is discussed. The key feature of the computational homogenization framework is the generality and accuracy compared to other homogenization schemes and the computational homogenization framework is efficient compared to DNS as showed in previous work [6]. The full scale problem is decomposed into two scales: the macroscopic scale and the microscopic scale. The macroscopic scale is the coarse scale and the microscopic scale is the fine scale, which can contain complex structures and non-linearity. At the macroscopic scale, the model consists of elements wherein each integration point a microscopic simulation is performed. The macroscopic scales supplies the microscopic scale with the macroscopic displacements and the deformation gradient. These macroscopic values are required to determine the microscopic initial conditions and boundary conditions. The microscopic scale supplies the macroscopic scale with the tangents, stresses and momentum. This process is schematically shown in Figure 4.4.

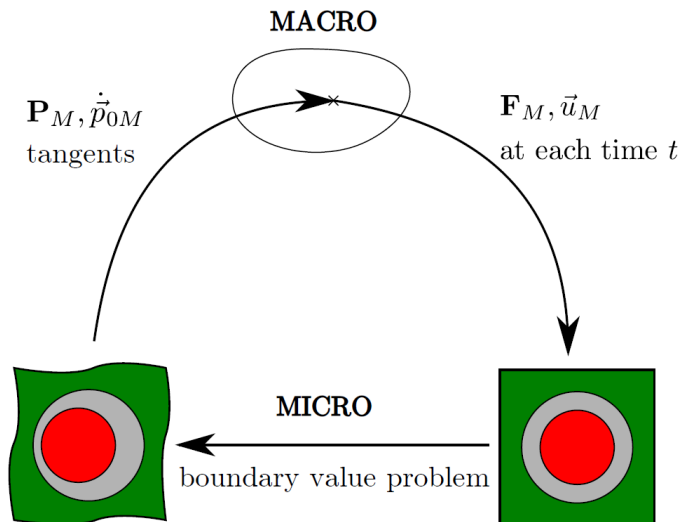


Figure 4.4: Schematic representation of the dynamic homogenization scheme. Reprinted from [5].

4.2.1 Macroscopic problem

The macroscopic discretized system of equations that needs to be solved is expressed as:

$$\mathbf{r}_M(\mathbf{x}_M) = \mathbf{f}_{M,inertia}(\mathbf{x}_M) + \mathbf{f}_{M,int}(\mathbf{x}_M) - \mathbf{f}_{M,ext} = \mathbf{0}, \quad (4.7)$$

where \mathbf{r}_M is the residual, $\mathbf{f}_{M,inertia}$ are the nodal inertia forces, $\mathbf{f}_{M,int}$ are the internal forces and $\mathbf{f}_{M,ext}$ are the external forces. The residual only vanishes if the balance of forces is satisfied. The inertia, internal and external forces are expressed as:

$$\mathbf{f}_{M,inertia}(\mathbf{x}_M) = \int_{V_0^M} N_0 \dot{\mathbf{p}}_{0M}(\mathbf{x}_{0M}) dV_{0M}, \quad (4.8)$$

$$\mathbf{f}_{M,int}(\mathbf{x}_M) = \int_{V_0^M} \nabla_{0M} N_0 \cdot \mathbf{P}_M^T(\mathbf{x}_M) dV_{0M}, \quad (4.9)$$

$$\mathbf{f}_{M,ext} = \int_{\Gamma_{0M}^h} N_0 \mathbf{t}_{0M}(\mathbf{X}_{0M}) d\Gamma_{0M}. \quad (4.10)$$

Here, V_{0m} is the initial (undeformed) volume of the model, \mathbf{t}_{0M} is the traction on the initial boundary layer Γ_{0M} . These equations are evaluated using isoparametric transformation and numerical integration via the Gauss quadrature, which is also done in Equations (8.3) - (8.8). The macroscopic stress \mathbf{P}_M and macroscopic momentum rate $\dot{\mathbf{p}}_{0M}$ are obtained from the microscopic scale. Therefore, these quantities need to be evaluated at the integration points, and a microscopic simulation has to be performed.

4.2.2 Microscopic problem

A periodic 1D unit cell on the microscopic scale is chosen since the LRAM consists of a periodic structure. Figure 4.5 shows schematically the representation of the 1D unit cell used in this project. The geometrical and material properties are the same as for the DNS and can be found in Table 4.1.



Figure 4.5: Schematic representation of the 1D unit cell used for the computational homogenization simulations. P^1 and P^2 indicate the prescribed boundary nodes.

The microscopic discretized system of equations that needs to be solved is expressed as:

$$\mathbf{r}_m = \mathbf{M}_m \cdot \ddot{\mathbf{u}}_m + \mathbf{f}_{m,int}(\mathbf{x}_m) - \mathbf{f}_{m,ext} = \mathbf{0}. \quad (4.11)$$

The difference between the macro and microscale is that at the latter the constitutive relation is known. The internal and external forces are determined in the same way as in the macroscopic scale with the difference that the microscopic units are used instead of macroscopic units. This is also the case for the mass matrix.

Equation 4.11 is first discretized in time, then solved via the same procedure as described in Table 2.4 and 2.5 for the standard scheme and composite scheme, respectively.

The boundary condition on the macroscale are equal to the boundary conditions for the DNS simulations. Instead of prescribed displacement on the first and last unit cell in the DNS simulations, the first and last node on macroscopic scale are prescribed.

The initial conditions are equal for both scales, which are equal to the DNS simulations: starting from rest.

The microscopic boundary conditions are calculated from the macroscopic deformation and macroscopic displacement as [6]:

$$\mathbf{u}_m^p = \mathbf{u}_M + (\mathbf{X}_{0m}^p - \mathbf{X}_{0m}^r) \cdot (\mathbf{F}_M^T - \mathbf{I}). \quad (4.12)$$

Here, p denotes the prescribed nodes p^1 and p^2 from Figure 4.5 for the first and last node, respectively. In previous work [5, 6], the boundary condition on the prescribed velocity and acceleration nodes are determined by taking the time derivative of Equation 4.12, resulting in:

$$\dot{\mathbf{u}}_m^p = \dot{\mathbf{u}}_M + (\mathbf{X}_{0m}^p - \mathbf{X}_{0m}^r) \cdot \nabla_{0M} \dot{\mathbf{u}}_M, \quad (4.13)$$

$$\ddot{\mathbf{u}}_m^p = \ddot{\mathbf{u}}_M + (\mathbf{X}_{0m}^p - \mathbf{X}_{0m}^r) \cdot \nabla_{0M} \ddot{\mathbf{u}}_M. \quad (4.14)$$

4.2.3 Macroscopic stress, momentum and tangents

The macroscopic stress \mathbf{P}_M and momentum $\dot{\mathbf{p}}_{0M}$ are used to determine the macroscopic internal forces and inertia forces, respectively. Therefore, these parameters are calculated at each (macroscopic) integration point after the microscopic simulation. The macroscopic stress and momentum rate are determined via [6]:

$$\mathbf{P}_M^T = \frac{1}{V_{0m}} \sum_{i=P^1, P^2} (\mathbf{X}_{0m}^i - X_{0m}^r) \mathbf{f}_{ext}^i, \quad (4.15)$$

$$\dot{\mathbf{p}}_{0M} = \frac{1}{V_{0m}} \sum_{i=P^1, P^2} \mathbf{f}_{ext}^i, \quad (4.16)$$

where \mathbf{X}_{0m}^i are the initial coordinates belonging to the prescribed boundary nodes, X_{0m}^r is the geometrical center of the RVE and \mathbf{f}_{ext}^i the external forces on these prescribed corner nodes.

In the dynamic computational homogenization framework, four tangents are required to describe the macroscopic material behaviour. The macroscopic tangent matrices ${}^4\mathbf{C}_M^{(1)}$, ${}^3\mathbf{C}_M^{(2)}$, ${}^3\mathbf{C}_M^{(3)}$, ${}^2\mathbf{C}_M^{(4)}$ are derived by condensation of the microscopic stiffness [6]. The tangents relate a virtual change in stress $\delta\mathbf{P}_M^T$ and momentum rate $\delta\dot{\mathbf{p}}_{0M}$ to deformation $\delta\mathbf{F}_M^T$ and rigid body displacement $\delta\mathbf{u}_M$ by:

$$\delta\mathbf{P}_M^T = {}^4\mathbf{C}_M^{(1)} : \delta\mathbf{F}_M^T + {}^3\mathbf{C}_M^{(2)} \cdot \delta\mathbf{u}_M, \quad (4.17)$$

$$\delta\dot{\mathbf{p}}_{0M} = {}^3\mathbf{C}_M^{(3)} : \delta\mathbf{F}_M^T + {}^2\mathbf{C}_M^{(4)} \cdot \delta\mathbf{u}_M. \quad (4.18)$$

The first macroscopic tangent stiffness, ${}^4\mathbf{C}_M^{(1)}$, relates the variation of macroscopic stress to the macrostructural deformation. ${}^4\mathbf{C}_M^{(1)}$ is expressed as:

$${}^4\mathbf{C}_M^{(1)} = \frac{1}{V_{0m}} \sum_{i=P^1, P^2} \sum_{j=P^1, P^2} (\mathbf{X}_{0m}^i - X_{0m}^r) \mathbf{S}_M^{*(ij)} (\mathbf{X}_{0m}^j - \mathbf{X}_{0m}^r), \quad (4.19)$$

with

$$\mathbf{S}_M^* = \left(\hat{\mathbf{K}}_m^{(pp)} \right)^* - \left(\hat{\mathbf{K}}_m^{(pf)} \right)^* \left(\left(\hat{\mathbf{K}}_m^{(ff)} \right)^* \right)^{-1} \left(\hat{\mathbf{K}}_m^{(fp)} \right)^*, \quad \text{such that } \mathbf{S}_M^* \delta\mathbf{u}_m^{(p)} = \delta\mathbf{f}_{ext}, \quad (4.20)$$

where the indices p and f denote the prescribed and free nodes, respectively and $\hat{\mathbf{K}}_m$ is the microscopic iteration matrix (definition can be found in Table 2.4 and 2.5).

The tangent ${}^3\mathbf{C}_M^{(2)}$ relates the macroscopic stress to the displacement variation. This tangent can be determined via:

$${}^3\mathbf{C}_M^{(2)} = \frac{1}{V_{0m}} \sum_{i=P^1, P^2} \sum_{j=P^1, P^2} (\mathbf{X}_{0m}^i - \mathbf{X}_{0m}^r) \mathbf{S}_M^{*(ij)}. \quad (4.21)$$

The next tangent, ${}^3\mathbf{C}_M^{(3)}$, relates the variation of macroscopic momentum to the macrostructural deformation. ${}^3\mathbf{C}_M^{(3)}$ is given by:

$${}^3\mathbf{C}_M^{(3)} = \frac{1}{V_{0m}} \sum_{i=P^1, P^2} \sum_{j=P^1, P^2} \mathbf{S}_M^{*(ij)} (\mathbf{X}_{0m}^j - \mathbf{X}_{0m}^r). \quad (4.22)$$

The last tangent relates the variation of macroscopic momentum to the displacement variation. ${}^2\mathbf{C}_M^{(4)}$ is expressed as:

$${}^2\mathbf{C}_M^{(4)} = \frac{1}{V_{0m}} \sum_{i=P^1, P^2} \sum_{j=P^1, P^2} \mathbf{S}_M^{*(ij)}. \quad (4.23)$$

4.3 Constitutive relations

Nonlinear material behaviour is incorporated in the dynamical homogenization scheme by means of constitutive relations. The epoxy and lead parts of the RVE have a linear elastic material model since the deformation of these parts are relatively small. However, in the rubber parts, the deformation can become large, especially for excitation frequencies inside the band gap. Therefore, the rubber parts are modelled with three material models: linear elastic, cubic and Neo-Hookean.

4.3.1 Linear elastic

The linear elastic material model is applied to the epoxy and lead parts in the RVE, and, when chosen, for the rubber parts. The latter is mainly used for comparison and validation purposes. The small strain assumption is applied which holds that the first Piola-Kirchhoff stress \mathbf{P} is equal to the Cauchy stress tensor $\boldsymbol{\sigma}$. In the 1D RVE, the stresses in transverse directions are assumed to be zero, $P_{22} = P_{33} = 0$, resulting in:

$$P \approx \sigma = Ee, \quad (4.24)$$

where e is the linear strain, expressed as $e = \lambda - 1$, with λ the stretch. Figure 4.6 shows the linear elastic constitutive behaviour (with the other constitutive models).

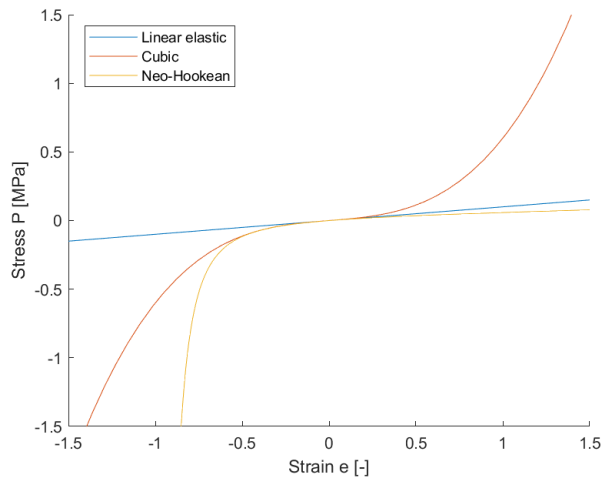


Figure 4.6: Stress-strain curves for the three considered material models describing the rubber constitutive behaviour. Inspired from [5].

4.3.2 Cubic

The cubic material model is the first nonlinear model considered in this project. Previous work [30] investigated the influence of the cubic material model in wave propagation in LRAMs, therefore it is considered in this project. The cubic material model is obtained by adding a nonlinear term to the linear material model:

$$P = Ee + \alpha Ee^3, \quad (4.25)$$

where α is the parameter controlling the nonlinearity. In this project, α is fixed as 5 (the same value as in previous work). For very small strains, the model is similar to the linear model which can be seen in Figure 4.6. For larger strains, the cubic model is antisymmetric (also referred to as odd function) and shows increase in stiffness for both compression and tension.

4.3.3 Neo-Hookean

Rubber materials are generally described by a hyperelastic material model. Therefore, in this project, the often used Neo-Hookean model is also considered. The 1D constitutive model for the incompressible Neo-Hookean is expressed as:

$$P = 2C_{10} \left(\lambda - \frac{1}{\lambda^2} \right), \quad (4.26)$$

where $\lambda = e + 1$. The stresses in transverse directions are assumed to be zero, $P_{22} = 0$ and $P_{33} = 0$. The material parameter C_{10} is obtained by requiring that the Neo-Hookean model is equal to the linear elastic model for small strains:

$$P = 6C_{10}e = Ee. \quad (4.27)$$

Thus, the material parameter $C_{10} = \frac{1}{6}E$. In Figure 4.6, the Neo-Hookean constitutive model can be seen. The figure shows that this model has an asymptotic behaviour for large compressive deformations at $e = -1$, which causes infinite compressive stress and tangent stiffness.

4.4 Boundary conditions for composite time integration schemes

In Section 4.2.4 the microscopic boundary conditions are given. For a standard time integration scheme, these can be used. However, when a composite time integration scheme is used, the time derivative can be different depending in which macroscopic sub step the simulation is in. For the trapezoidal rule (or other standard schemes), there is no difference since the macroscopic scale has the same time integration scheme as the microscopic scale. In the composite schemes, the time steps are not synced. For example, if the Bathe scheme is used, the first sub step is the trapezoidal rule and the second is the backward Euler. If the macroscopic scale is in the first sub step and the microscopic scale is solved via the Bathe scheme, then in the second sub step at microscopic scale, backward Euler is used while the macroscopic scale is solving the system with the trapezoidal rule. Therefore, the macroscopic displacements cannot be used to determine the microscopic prescribed velocities and accelerations. This can also be proven with the time integration equations and Equation 4.12. The prescribed velocity can also be determined via time integration at the microscopic scale as:

$$\mathbf{v}_m^p = \frac{\partial}{\partial t}(\mathbf{u}_m^p), \quad (4.28)$$

where \mathbf{u}_m^p is the prescribed displacement from Equation 4.12 and \mathbf{v}_m^p the microscopic time derivative of \mathbf{u}_m^p . Note that the latter is chosen with a \mathbf{v} such that it is visually different from the prescribed microscopic velocity from Equation 4.13. For clarity, the times T_0 , T_1 and T_2 are introduced which describe the macroscopic initial time t , the time at the first sub step $t + \Delta t/2$ and the time at the second sub step $t + \Delta t$, respectively. The same is done for the times at the microscopic scale, t_0 describes the initial time, t_1 the time at the first sub step and t_2 the time at the second sub step.

At the macroscopic scale, in the first sub step, the microscopic simulation is run with the Bathe scheme. In the first sub step in the microscopic scale, the prescribed velocity can be determined via Equation 4.13:

$$\begin{aligned} {}^{t_1}\dot{\mathbf{u}}_m^p &= \dot{\mathbf{u}}_M^{T_1} + (\mathbf{X}_{0m}^p - X_{0m}^r) \cdot \nabla_{0M} \dot{\mathbf{u}}_M^{T_1}, \\ &= \frac{4}{\Delta t} \mathbf{u}_M^{T_1} - \frac{4}{\Delta t} \mathbf{u}_M^{T_0} - \dot{\mathbf{u}}_M^{T_0} + (\mathbf{X}_{0m}^p - X_{0m}^r) \cdot \nabla_{0M} \left(\frac{4}{\Delta t} \mathbf{u}_M^{T_1} - \frac{4}{\Delta t} \mathbf{u}_M^{T_0} - \dot{\mathbf{u}}_M^{T_0} \right). \end{aligned} \quad (4.29)$$

The prescribed velocity can also be determined via the other method as:

$${}^{t_1}\mathbf{v}_m^p = \frac{4}{\Delta t} \mathbf{u}_m^{t_1} - \frac{4}{\Delta t} \mathbf{u}_m^{t_0} - \dot{\mathbf{u}}_m^{t_0}. \quad (4.30)$$

When comparing Equation 4.29 to Equation 4.30, the same integration constants are used for the different terms and therefore they are equivalent. Note that this is basically what happens with the trapezoidal rule if instead of a sub step a full time step is taken. However, in the second sub step at microscopic scale, the Bathe scheme uses the backward Euler method. At macroscopic scale nothing changes and the microscopic velocity is calculated the same:

$${}^{t_2}\dot{\mathbf{u}}_m^p = \dot{\mathbf{u}}_M^{T_1} + (\mathbf{X}_{0m}^p - X_{0m}^r) \cdot \nabla_{0M} \dot{\mathbf{u}}_M^{T_1}, \quad (4.31)$$

$$= \frac{4}{\Delta t} \mathbf{u}_M^{T_1} - \frac{4}{\Delta t} \mathbf{u}_M^{T_0} - \dot{\mathbf{u}}_M^{T_0} + (\mathbf{X}_{0m}^p - X_{0m}^r) \cdot \nabla_{0M} \left(\frac{4}{\Delta t} \mathbf{u}_M^{T_1} - \frac{4}{\Delta t} \mathbf{u}_M^{T_0} - \dot{\mathbf{u}}_M^{T_0} \right). \quad (4.32)$$

The other methods calculates the prescribed velocities at microscopic scale via the second sub step, using the backward Euler method as:

$${}^{t_2}\mathbf{v}_m^p = \frac{1}{\Delta t} \mathbf{u}_m^{t_0} + \frac{-4}{\Delta t} \mathbf{u}_m^{t_1} + \frac{3}{\Delta t} \mathbf{u}_m^{t_2} \quad (4.33)$$

Now, when comparing these two equations, a difference is observed and these are not equivalent. Therefore, the boundary conditions at microscopic scale for the velocities and accelerations need to be applied in a different method when using a composite scheme.

One way of applying the prescribed velocities and accelerations to the system, is treating the prescribed velocities and accelerations as ‘free’ nodes and updating the nodes depending on the prescribed displacement. The prescribed displacement are used in this method as initial conditions instead of boundary conditions where the change in prescribed displacement is determined at (for instance) the first microscopic time step as:

$$\Delta \mathbf{u}_m^{p,t+\Delta t/2} = (\mathbf{u}_m^{p,t+\Delta t/2} / 2 - \mathbf{u}_m^{p,*,t+\Delta t/2}), \quad (4.34)$$

where $\mathbf{u}_m^{p,t+\Delta t/2}$ is the prescribed displacement calculated with Equation 4.12 and $\mathbf{u}_m^{p,*,t+\Delta t/2}$ the guessed displacement. The guessed displacement is the same as for the ‘free’ nodes (see Table 2.5) and depend on the sub step. In this case, the guessed displacement are expressed as:

$$\mathbf{u}_m^{p,*,t+\Delta t/2} = \mathbf{u}^t + \frac{\Delta t}{4} \dot{\mathbf{u}}^t + \frac{(\Delta t)^2}{16} \ddot{\mathbf{u}}^t, \quad (4.35)$$

Then, the prescribed velocities are determined via the guessed prescribed velocities $\dot{\mathbf{u}}_m^{p,*,t+\Delta t/2}$ and the correction in displacement as:

$$\dot{\mathbf{u}}_m^{p,t+\Delta t/2} = \dot{\mathbf{u}}_m^{p,*,t+\Delta t/2} + \frac{4}{\Delta t} \Delta \mathbf{u}_m^{p,t+\Delta t/2}. \quad (4.36)$$

The same method is applied to the prescribed accelerations:

$$\ddot{\mathbf{u}}_m^{p,t+\Delta t/2} = \ddot{\mathbf{u}}_m^{p,*,t+\Delta t/2} + \frac{16}{\Delta t^2} \Delta \mathbf{u}_m^{p,t+\Delta t/2}, \quad (4.37)$$

where the guess $\ddot{\mathbf{u}}_m^{p,*,t+\Delta t/2}$ is zero.

4.5 Time integration scheme on the microscopic scale

Using a composite time integration scheme on the microscopic scale introduces new challenges. As mentioned above, the boundary conditions are defined differently. In addition, the external forces and therefore the acceleration are important since they are used to calculate the macroscopic stress and momentum. Currently, no macroscopic convergence can be reached when using a composite time integration scheme on the microscopic scale. There is microscopic convergence, however, the calculated microscopic accelerations deviate from the microscopic accelerations calculated with the trapezoidal rule, which does reach microscopic and macroscopic convergence. The cause of this problem could not be found during this project. For the computational homogenization results, on the macroscopic scale the three different time integration schemes are employed. On the microscopic scale only the trapezoidal rule is used.

4.6 Simulation approach

In the next two chapters, the DNS and computational homogenization results are shown, respectively. Simulations are performed for multiple cases: one DNS and multiple homogenization simulations. In the DNS simulation, 3360 unit cells are used. The simulation is simulating up to 0.1 s, with a time step of $\Delta t = 0.0001$ s. In Figure 4.7, a schematic representation of the simulations is shown. The macroscopic scale in the computational homogenization has the same length l_M as the DNS simulations. In the homogenization simulations, the homogenization level h is varied by changing the number of macroscopic integration points. The homogenization level h is defined as the ratio between the number of DNS unit cells and the number of integration points at the macroscopic scale.

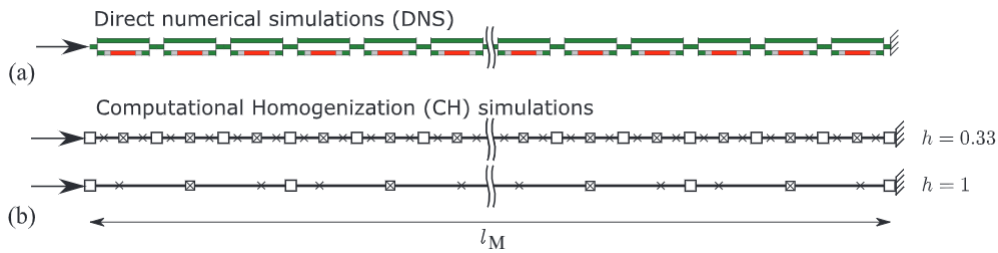


Figure 4.7: Schematic representation of the 1D simulations. The top picture indicates one DNS simulation. The bottom two pictures indicate homogenization simulations with different amounts of homogenization. From top to bottom: $h = 0.33$, $h = 1$. Here, at each integration point indicated by the crosses, a microscopic simulation is performed. Reprinted from [6].

Chapter 5

Direct numerical simulations

In this chapter, the time integration schemes are used to solve the Direct Numerical Simulations (DNS) of the LRAM. First, the results for the linear material model are shown. Then, the cubic and Neo-Hookean material model results are discussed. Finally, a comparison between linear elements and quadratic elements is shown.

5.1 Linear constitutive model

In this section, the results of the DNS with the linear constitutive model are shown. In Figure 5.1, the transmissibility is shown. The transmissibility θ is expressed as:

$$\theta = \frac{B(\frac{1}{4}l_M)}{B(0)}, \quad \text{with} \quad B(x) = \sqrt{\frac{1}{\frac{1}{2}n_T} \sum_{n=\frac{1}{2}n_T}^{n_T} (u_n^x)^2}, \quad (5.1)$$

where $n_T = T/\Delta t$ is the total number of time steps during the simulation and u_n^x is the displacement of the epoxy at position x at time step n . Since $n_T/2$ is used, only the displacement of the second half of the simulation is taken into account. This compensates for the transient effects, which are present in the first time steps. Note that B can be described as root mean square (RMS) of the displacement. The transmissibility θ is determined for various input frequencies and visualized against each other in a transmissibility diagram shown in Figure 5.7. A transmissibility of 1 corresponds with a fully propagating wave, while a transmissibility of 0 corresponds with a wave that does not propagate. In this figure, the region where the transmissibility drops, is the band gap. The band gap is approximately between 125 and 275 Hz. Comparing the obtained band gap from the simulations with the calculated band gap of the RVE in Section 4.1 shows resemblance. For an input frequency above the band gap (e.g. 350 Hz), the transmissibility returns to 1. The numerical damping in the Bathe and Wen scheme are not noticeable in the displacements since the transmissibility are equal with the trapezoidal rule where the damping effect is absent. However, comparison to the benchmark problem results in the same observation, the displacement is comparable while the velocity and accelerations are different between the schemes due to the numerical damping.

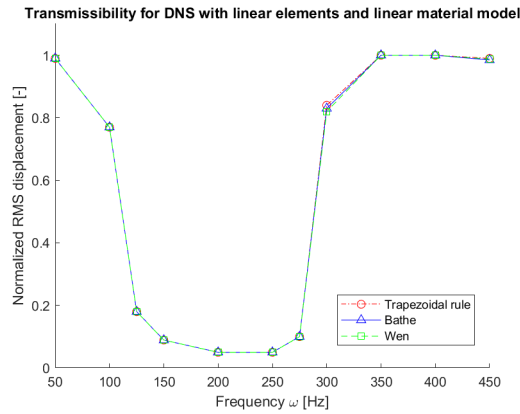


Figure 5.1: Transmissibility of the system with a linear material model for the trapezoidal rule, Bathe scheme and Wen scheme.

Three different frequencies are considered: one below the band gap, one inside the band gap and one above the band gap; 50, 200 and 350 Hz, respectively. For each frequency, the results are shown for the three different materials (see Figure 5.2 for considered node positions); the middle node of the lead part (C), the middle node of the left rubber part (B) and the middle node of the upper layer epoxy part (A).

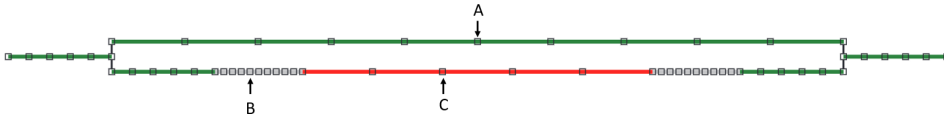


Figure 5.2: The considered unit cell with the considered nodes for the DNS results. Node ‘A’ is the upper epoxy node, node ‘B’ is the rubber node and node ‘C’ is the considered lead node.

The following graphs show the results in the space domain at time $t = 0.074$ s, $t = 0.064$ s and $t = 0.054$ s for below the band gap, inside the band gap and above the band gap, respectively. At these specific times, the wave is not yet reflected. However, the transient effects are still present. The transient effects are coming from two phenomenons present in the system. First, the initial and boundary conditions for the velocities do not match. The velocity jumps to the prescribed value after the initial condition. According to (4.5) the initial condition for the velocity is zero, while the boundary condition describes a velocity of $B \cos(Ct)$, which does not equal 0 at $t = 0$. Since this mismatch is relatively large, the integration schemes have trouble describing this. Secondly, these transient effects have a high velocity and small amplitude. The error between the numerical and analytical wave velocity is a function of the wavenumber [31, 32]. Since the wavenumber is different in the transient effect, the error is higher, resulting in these high frequency spurious modes. The Bathe and Wen scheme have numerical damping incorporated. However, the numerical damping has the largest influence for very large errors and these transient effect do not fall into this category.

The normalized displacement of the upper epoxy part can be seen in Figure 5.3. The displacement is normalized by diving the displacement with the imposed amplitude of the wave. All three schemes scheme show no high frequency spurious modes in all three frequencies. The trapezoidal rule shows different displacements in the transient region (in the figure, this region is at the right) for a frequency inside and above the band gap.

Figure 5.4 shows the normalized velocity of the upper epoxy part. The velocity is normalized by diving the velocity with the imposed amplitude of the wave times the imposed frequency. In these figures, the differences between the schemes are more easily observed, especially with a frequency inside the band gap. Here, the same phenomena is observed as in the benchmark problem where the trapezoidal rule shows high frequency spurious oscillations. In the other frequencies, this effect is mostly observed

in the transient region, where all three schemes show these high frequency spurious modes. The displacement of the rubber part can be seen in Figure 5.5. The same can be observed as for the displacement of the epoxy. The Bathe and the Wen scheme show no spurious oscillations and the trapezoidal rule shows some spurious oscillations in the transient region. Figure 5.6 shows the velocity of the rubber parts. The high frequency spurious modes phenomena is more present. Now, in the peaks, where the amplitude is the largest, the trapezoidal rule overshoots the other schemes. This can be explained by the numerical damping present in the Bathe and Wen scheme. Noh et al [32] describes that for unconditionally stable implicit time integration schemes, the amplitude of the numerical calculated wave decreases due to numerical damping. The exception is the trapezoidal rule, where the numerical damping is not present.

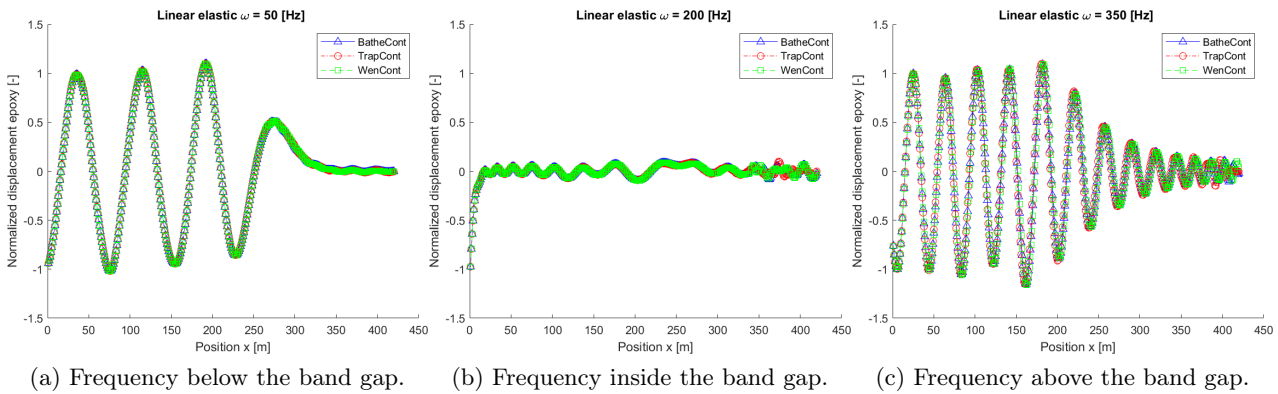


Figure 5.3: Comparison between the displacement of the upper epoxy part for frequencies below the band gap, above the band gap and above the band gap. The displacement is taken at (a) $t = 0.074$ s, (b) $t = 0.064$ s and (c) $t = 0.054$ s, before the wave reached the end of the system.

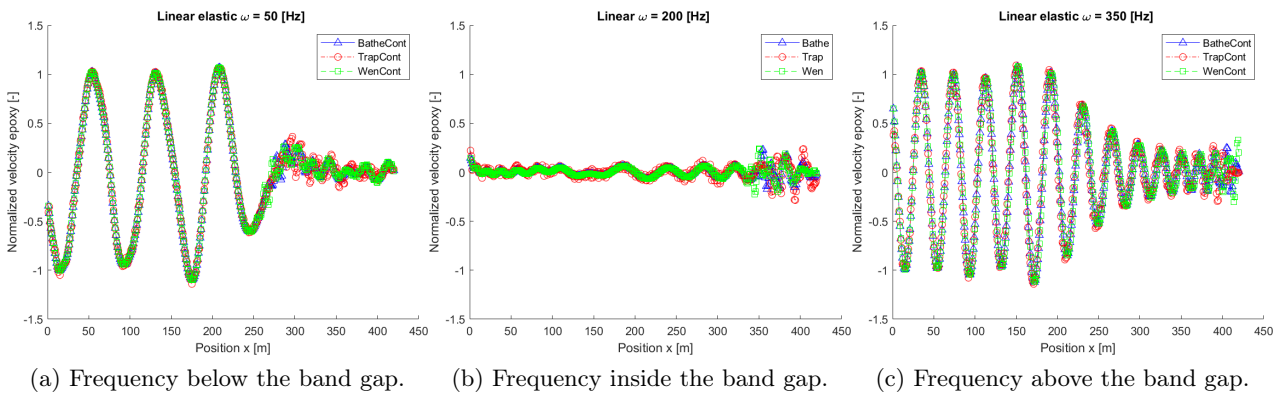


Figure 5.4: Comparison between the velocity of the upper epoxy part for frequencies below the band gap, inside the band gap and above the band gap. The velocity is taken at (a) $t = 0.074$ s, (b) $t = 0.064$ s and (c) $t = 0.054$ s, before the wave reached the end of the system.

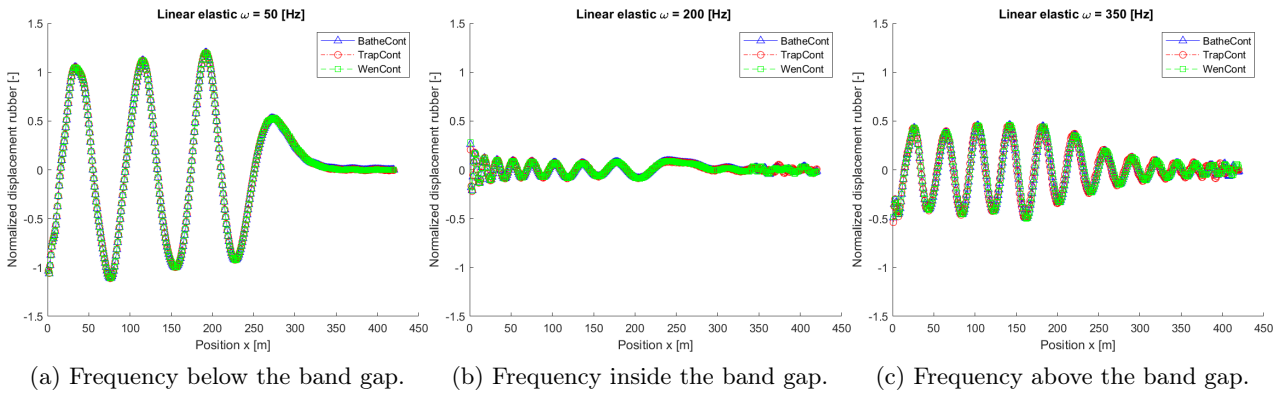


Figure 5.5: Comparison between the displacement of the rubber part for frequencies below the band gap, inside the band gap and above the band gap. The displacement is taken at (a) $t = 0.074$ s, (b) $t = 0.064$ s and (c) $t = 0.054$ s, before the wave reached the end of the system.

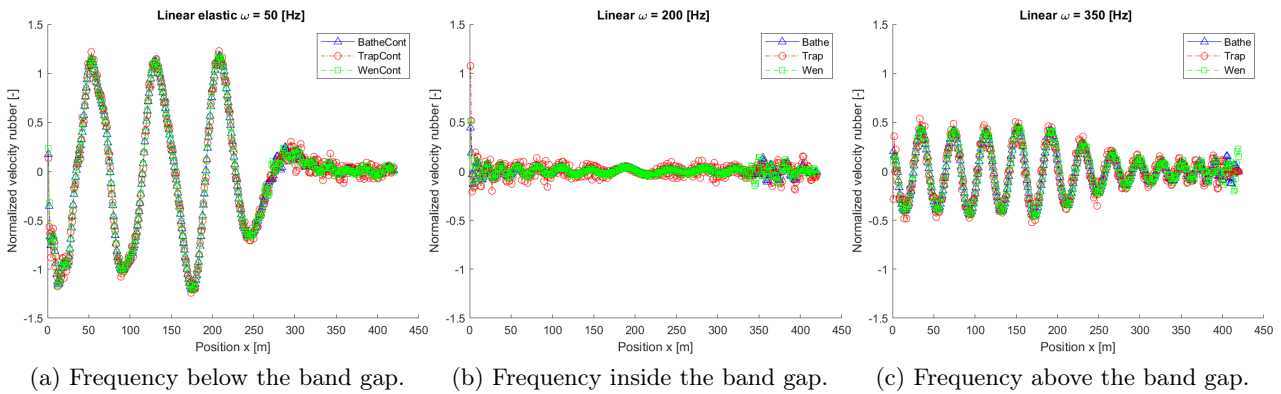


Figure 5.6: Comparison between the velocity of the rubber part for frequencies below the band gap, inside the band gap and above the band gap. The velocity is taken at (a) $t = 0.074$ s, (b) $t = 0.064$ s and (c) $t = 0.054$ s, before the wave reached the end of the system.

5.2 Cubic constitutive model

This section discusses the results of the DNS with the cubic material model. Figure 5.7 shows the transmissibility plot where the band gap can be seen. When this figure is compared to the linear elastic material model two differences are observed. First, the band gap is shifted to higher frequencies, and secondly, at the top of the band gap, the transition is much smoother. There is not a sudden jump to a transmissibility of 1 which is the case for the linear elastic one. The shift of the band gap for non-linear material models is a known phenomena in literature (see e.g. [33]). Since the band gap is shifted, the 'above' band gap result has a higher frequency as well, now this result is shown with a frequency of 550 Hz.

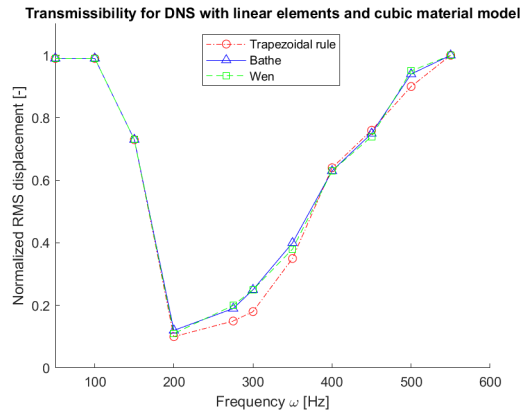
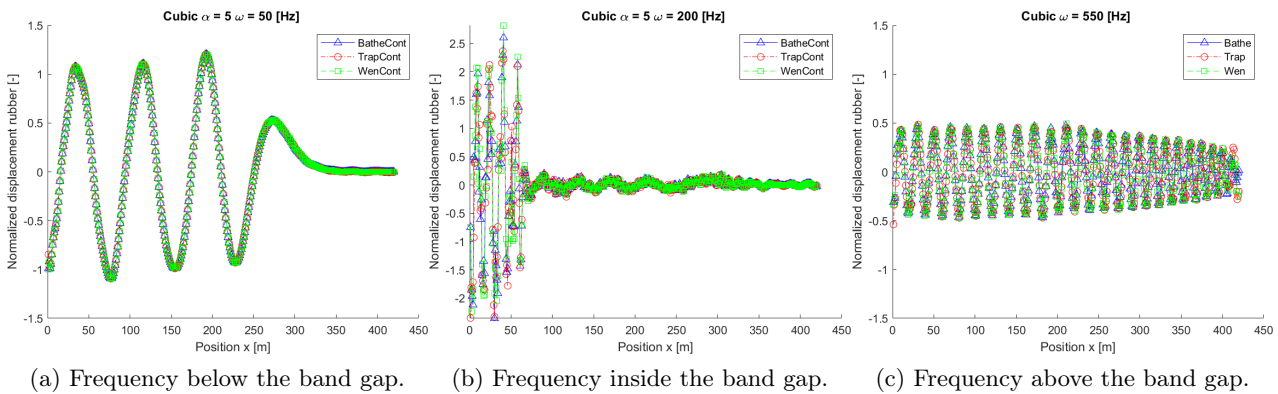


Figure 5.7: Transmissibility of the system with a cubic material model for the trapezoidal rule, Bathe scheme and Wen scheme.

Figure 5.8 shows the displacement of the rubber node (B in Figure 5.2) in the three considered frequencies. In the frequency below the band gap, all three schemes are capable of solving the problem without any spurious oscillations. Inside the frequency however, especially at the first few unit cells, all three schemes show high frequency spurious oscillations. At this position, the stresses are the largest in the rubber, resulting in this behaviour. Figure 5.10 shows the stress-displacement curve of the first node. It can be seen that the stresses in the trapezoidal rule are considerably larger than for the other schemes. The stresses are used in the model to evaluate the residual (Equation (4.11)) with the momentum term. The momentum term contains the accelerations. Since the accelerations show these high spurious oscillations they compensate for the high stresses in the model, therefore convergence is reached.

The velocity of the rubber node can be seen in Figure 5.9. The same is observed for the velocity of the rubber node in case of a linear elastic model; the trapezoidal shows spurious oscillations in the transient regime. If the frequency is inside the band gap, all three schemes show additional spurious oscillations at the first few unit cells.



(a) Frequency below the band gap. (b) Frequency inside the band gap. (c) Frequency above the band gap.

Figure 5.8: Comparison between the displacement of the rubber part for frequencies below the band gap, inside the band gap and above the band gap. The displacement is taken at (a) $t = 0.074$ s, (b) $t = 0.064$ s and (c) $t = 0.054$ s, before the wave reached the end of the system.

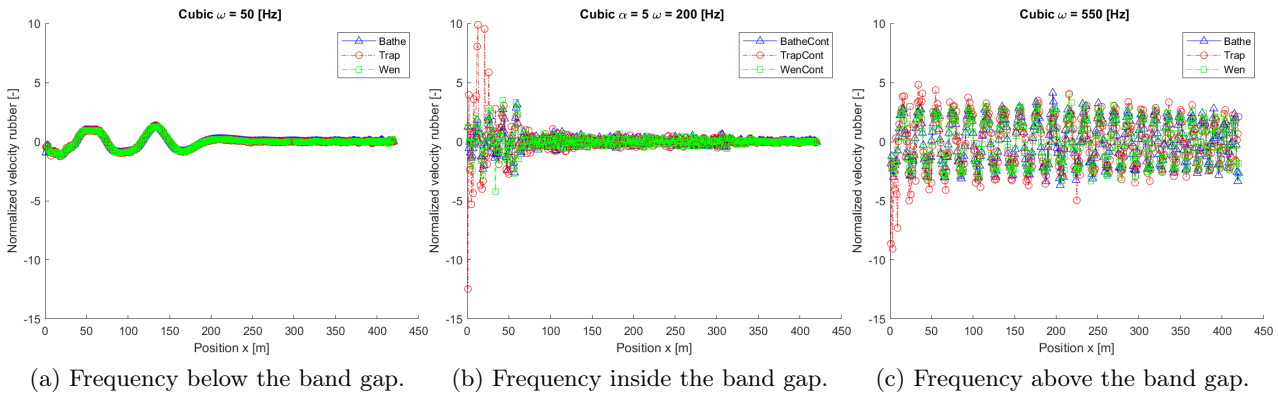


Figure 5.9: Comparison between the velocity of the rubber part for frequencies below the band gap, inside the band gap and above the band gap. The velocity is taken at (a) $t = 0.074$ s, (b) $t = 0.064$ s and (c) $t = 0.054$ s, before the wave reached the end of the system.

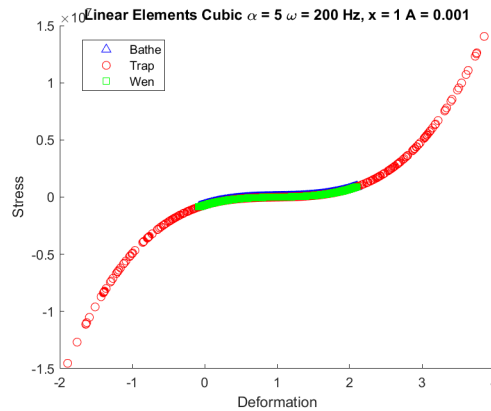


Figure 5.10: Stress-deformation curve for the first node for the three considered schemes.

5.3 Neo-Hookean constitutive model

This section discusses the results obtained with the non-linear Neo-Hookean material model. The simulations with the Neo-Hookean model showed a lot of instabilities. A very small time step of $1e-7$ s must be chosen to reach convergence when the input frequency is inside the band gap. Even when this time step is used, the rubber displacements are unrealistic. Frequencies below the band gap, i.e. 50 or 100 Hz, do not show these instabilities and can be solved with the same time step as with the linear elastic model.

Since the considered unit cell is (semi) 1D, the upper epoxy parts are not influenced by the rubber displacements and therefore the transmissibility can be made. Figure 5.11 shows the transmissibility for the Neo-Hookean material model for the three considered schemes. The same phenomena is observed as with the cubic material model where the band gap is shifted to higher frequencies. Since the results for an input frequency inside the band gap are questionable, the only meaningful part is the transmissibility for an input frequency of 50 and 100 Hz. Here, all three schemes show the same transmissibility.

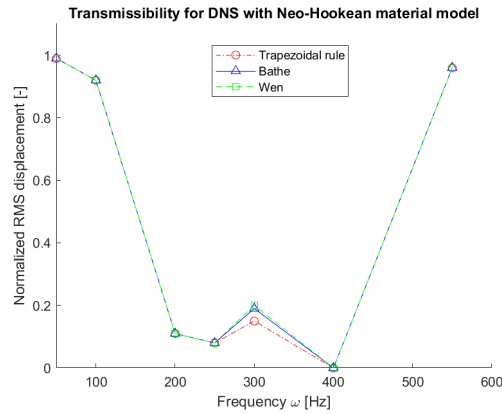


Figure 5.11: Transmissibility of the system with a Neo-Hookean material model for the trapezoidal rule, Bathe scheme and Wen scheme.

Figure 5.12 shows the rubber displacements for the three considered frequencies, below, inside and above the band gap. Below the band gap, the three schemes are similar and the results are comparable with the obtained results for the linear and cubic material model. For an input frequency inside the band gap, the displacement with the Bathe scheme shows a high spurious oscillation. The other two schemes do not show these spurious oscillations. However, when a different frequency is considered, the other schemes also show these spurious oscillations. The spurious oscillations are increasing for an increasing frequency. When the frequency is at 550 Hz, the rubber displacements are unrealistic, as can be seen in Figure 5.12(c). The displacement of the lead part also shows unrealistic values and spurious oscillations. In the linear and cubic material model this is not the case.

Figure 5.13 shows the velocity of the rubber node. As expected, the same is observed for the velocity as for the displacement. Below the band gap, the velocity is comparable to the linear and cubic material model and all three schemes are similar. In side and above the band gap, high frequency spurious modes are observed.

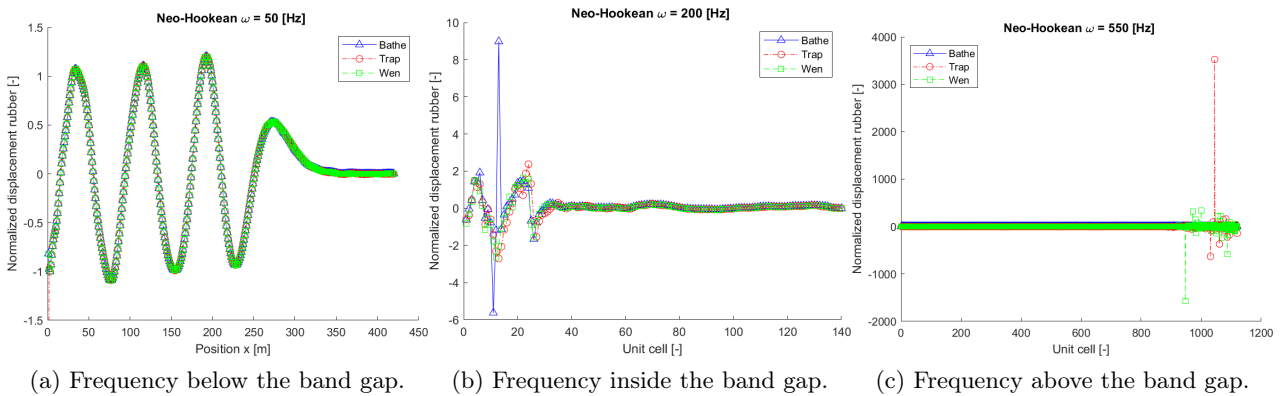


Figure 5.12: Comparison between the displacement of the rubber part for frequencies below the band gap, inside the band gap and above the band gap. The displacement is taken at (a) $t = 0.074$ s, (b) $t = 0.064$ s and (c) $t = 0.054$ s, before the wave reached the end of the system. Note the difference in the axis for plot (c).

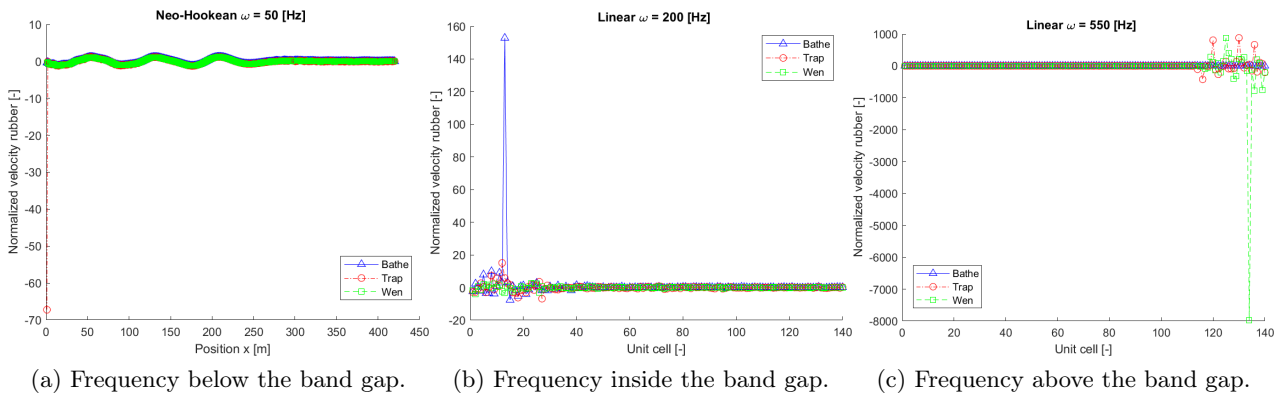


Figure 5.13: Comparison between the velocity of the rubber part for frequencies below the band gap, inside the band gap and above the band gap. The velocity is taken at (a) $t = 0.074$ s, (b) $t = 0.064$ s and (c) $t = 0.054$ s, before the wave reached the end of the system. Note the difference in the axis for plot (c).

5.4 Discussion

In the simulations with the linear material model, no difference is observed in the displacement between the three considered schemes. In the velocity however, there are high frequency spurious modes for the trapezoidal rule, especially for an input frequency inside the band gap. In the acceleration, these spurious oscillations are even more profound, matching the obtained results in the benchmark problem where the acceleration with the trapezoidal also show these spurious modes. However, this does not translate back to the displacement. In literature, multiple model problems are applied to the trapezoidal rule, Bathe and Wen scheme where the same results are observed. The trapezoidal rule shows high frequency spurious modes in the velocity and acceleration but these do not translate to the obtained displacements.

The simulations with the cubic material model shows a shift in the band gap. Also, the transmissibility plot shows a different value for the trapezoidal rule compared to the Bathe and Wen scheme at an input frequency of 200 to 350 Hz. This is caused by a few higher predictions for the displacement of the epoxy part. In general the Bathe and Wen scheme show no spurious oscillations. However, in some time steps, the Bathe and Wen scheme overestimate the displacement compared to the trapezoidal rule. Since the displacement is large in these time steps, the transmissibility is larger.

As mentioned before, the simulations with the Neo-Hookean material model show a lot of instabilities for an input frequency inside and above the band gap. These instabilities are caused by the transient effects present in the model. In previous work numerical damping is added to suppress these transient effects. In this work, the numerical damping was removed and the two composite schemes were added which have integrated numerical damping. However, the numerical damping in the composite scheme is unable to fully suppress these transient effects. In literature (see e.g. [11, 32]) model problems are shown where the use of the Bathe scheme is compared to the trapezoidal rule. The Bathe scheme does suppress high spurious modes, which can also be seen in the obtained results in this work. However, the literature also shows that the damping is linked to the relative wave speed error, spatial discretization and temporal discretization. Since the spatial and temporal discretization is not optimized for the transient effects, the transient effect are only slightly damped.

In future work, it is recommended to try a smaller amplitude to the prescribed wave. A smaller amplitude should reduce the stresses and therefore the model should be more stable.

Simulations are also performed with quadratic elements. However, no difference is observed with the use of quadratic elements. The spatial discretization in the unit cell is relatively small. The

increasing in spatial discretization can also be disadvantageous for the total accuracy on the results [32].

Chapter 6

Computational homogenization simulations

In this chapter, the time integration schemes are used to solve the Computational homogenization simulations of the LRAM. The DNS results are used as reference. First, the results for the linear material model are shown. Then, the cubic and Neo-Hookean material model results are discussed. Finally, the results with quadratic elements are shown.

6.1 Linear Elastic

The computational homogenization results are validated by comparing the macroscopic displacement of the homogenization simulation with $h = 1$ to the displacement of the corresponding direct numerical simulation. An equal number of unit cells is considered, which should result in equivalent results. Simulations have been performed with the linear elastic material model describing the rubber behaviour. The resulting displacement are shown for each integration scheme separately. Figure 6.1(a) shows the results with an frequency below the band gap, $\omega = 50$ Hz. The results are normalized with respect to the input amplitude (u/A). The CH results are shown for one in every 8 nodes to increase the clarity. Figures 6.1(b) and 6.1(c) show the comparison for an input frequency of 200 Hz and 350 Hz, inside and above the band gap, respectively. All three considered frequencies show matching results between the DNS and the CH simulations. Similar results have been obtained for other frequencies in the range of interest.

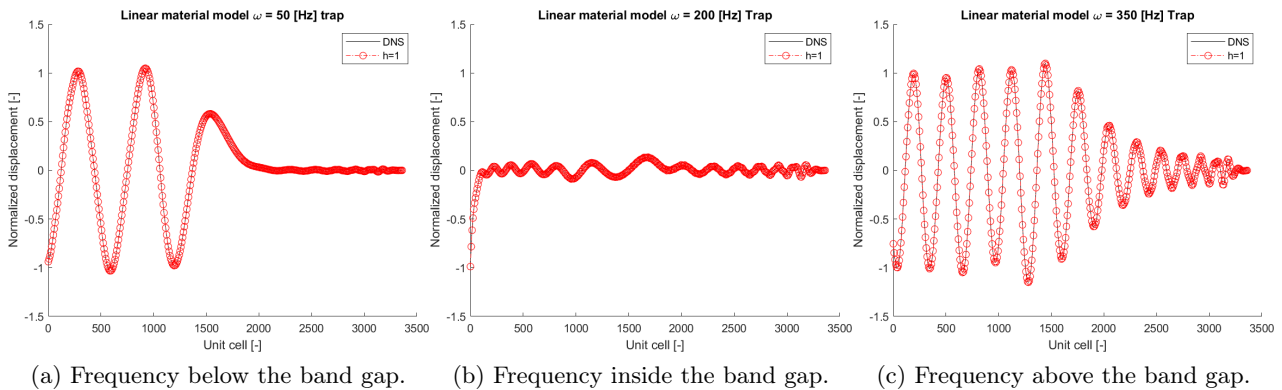


Figure 6.1: Comparison between the displacement via the trapezoidal rule for frequencies below the band gap, above the band gap and above the band gap. The displacement is taken at $t = 0.054$ s, before the wave reached the end of the system.

In Figure 6.2, the comparison between the DNS and computational homogenization results with a

homogenization level $h = 1$ is shown with the Bathe scheme for three input frequencies: 50, 200 and 350 Hz, below, inside and above the band gap, respectively. The results match in the steady-state region but in the transient region, discrepancies are seen. Note that previous chapter described problems with the composite schemes at microscale and therefore the trapezoidal rule is used in the microscale simulations. Hence, the discrepancies in these results.

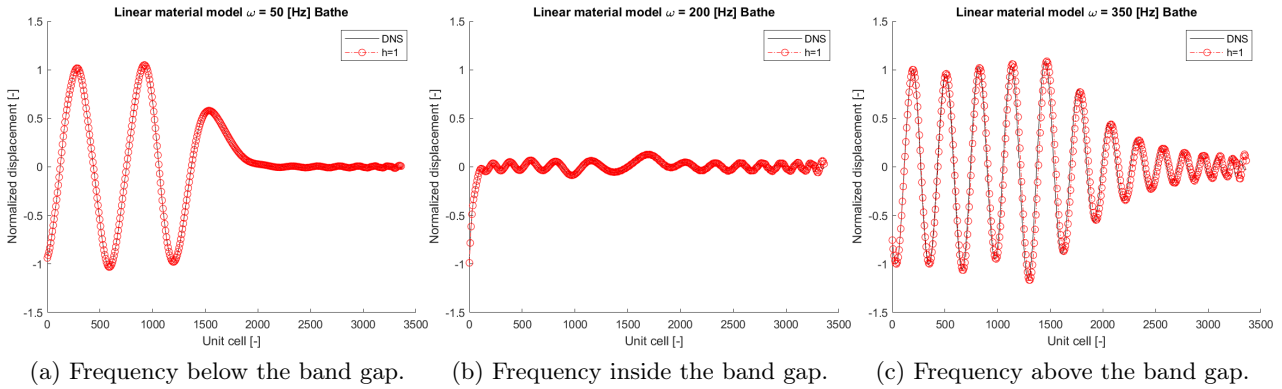


Figure 6.2: Comparison between the displacement via the Bathe scheme for frequencies below the band gap, above the band gap and above the band gap. The displacement is taken at $t = 0.054$ s, before the wave reached the end of the system.

Figure 6.3 shows the displacement of the DNS and the computational homogenization with a homogenization level $h = 1$ for the three considered frequencies with the Wen scheme. The same is observed for these results as for the results with the Bathe scheme; the steady-state response match but discrepancies are visible in the transient region. Again, this is caused by the use of the trapezoidal rule in the microscale simulations.

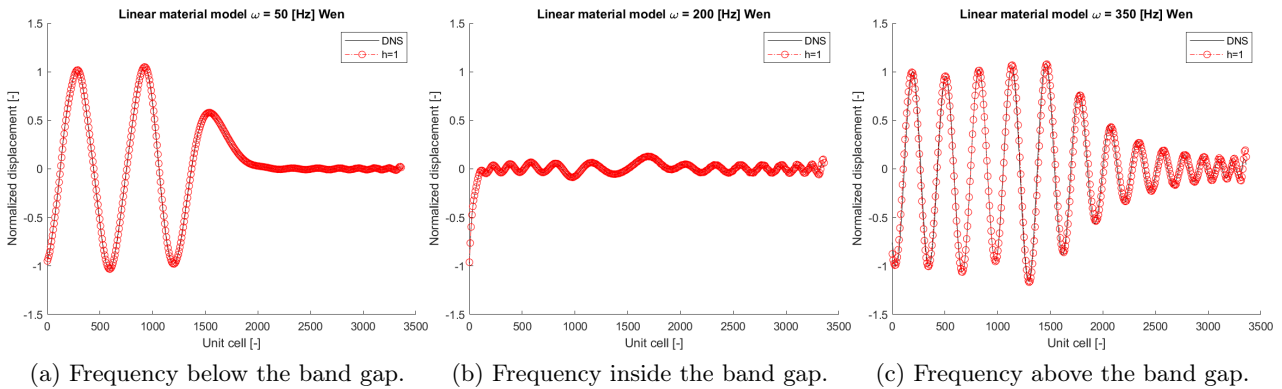


Figure 6.3: Comparison between the displacement via the Wen scheme for frequencies below the band gap, above the band gap and above the band gap. The displacement is taken at $t = 0.054$ s, before the wave reached the end of the system.

Figure 6.4 shows a comparison of the transmissibility for DNS and CH simulations with different homogenization levels h . Here, the black line indicates the DNS results and the colored dots the various homogenization results. Comparing the results of the three schemes shows matching results. The transmissibility is the same for all homogenization levels for the three schemes. Comparing this with the DNS and CH results substantiate the matching between the schemes. In the DNS and CH results no difference in the steady state regime is seen, therefore the transmissibility is also similar. There is however, a discrepancy between higher homogenization levels and the DNS results for a input frequency of 100 Hz. This is also seen in previous work [5] at exactly the same frequency, however,

direct comparison cannot be made since previous work included damping in each node, which is not the case here. Although direct comparison cannot be made, the cause of the discrepancy is the same; numerical dispersion. Figure 6.5 shows a comparison between the DNS and the CH results with a homogenization level of 20 and an input frequency of 100 Hz at time $t = 0.074$ s. A growing shift is observed between the DNS and CH results. The wavelength calculated by the homogenization results deviates from the DNS results, which causes a phase shift. A consequence of this phase shift is a difference in amplitude, resulting in a different transmissibility. This phase shift is found in all three schemes. Section 6.5 discusses this in more detail.

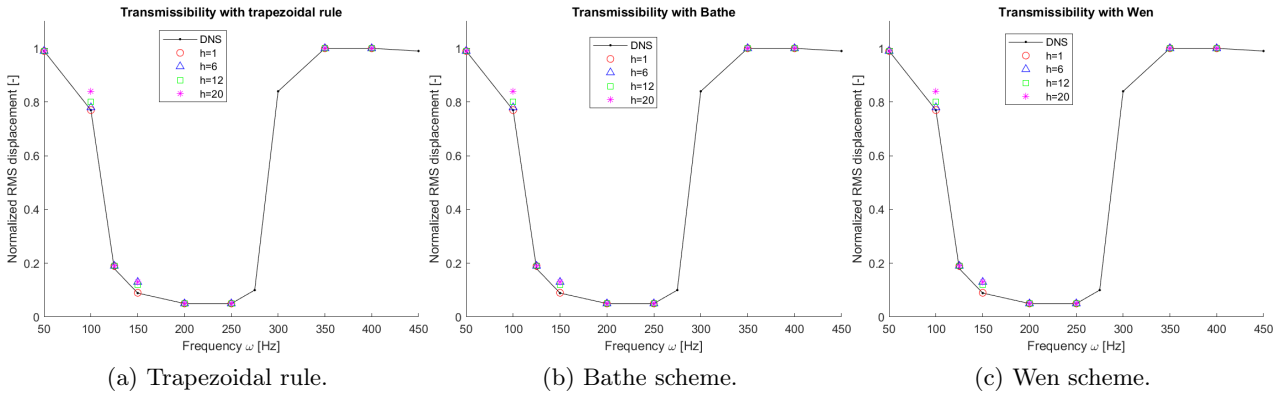


Figure 6.4: Transmissibility for the three considered time integration schemes. For each scheme, a comparison between the DNS and CH simulation with different homogenization levels is made for a variety of frequencies.

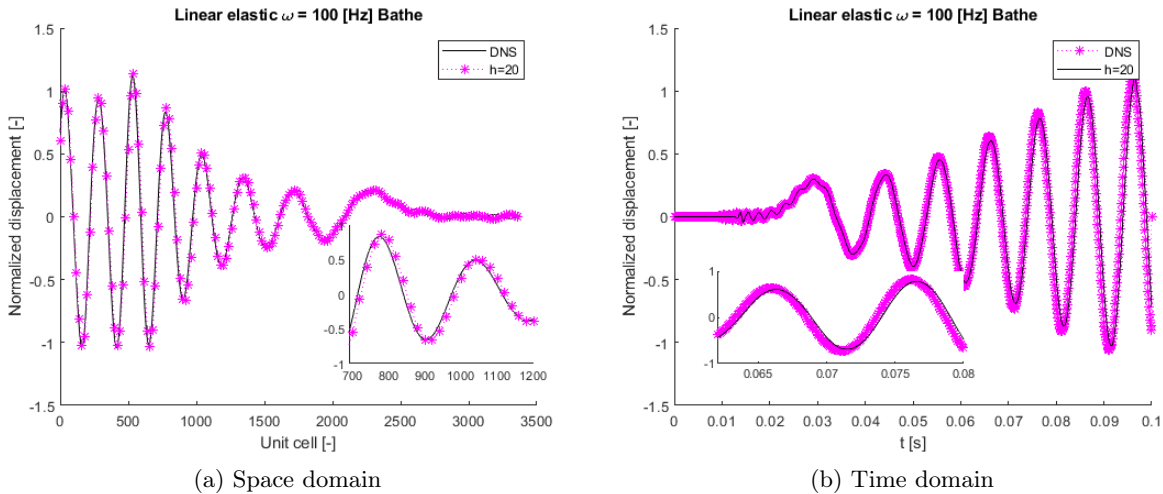


Figure 6.5: Comparison between the DNS and homogenization results for $h = 20$, with an input frequency of $\omega=100$ Hz in the (a) space domain at $t = 0.074$ s and (b) time domain at $x = \frac{1}{4}l_M$ for the Bathe scheme.

6.2 Cubic

The computational homogenization simulations are validated by comparison to the DNS simulations. Figure 6.6 shows a comparison between the DNS simulation and the computational homogenization simulation with a homogenization level of $h = 1$ for an input frequency of 50 Hz for the three considered schemes. It can be observed that for all three schemes the computational homogenization simulations

are accurately predicting the response for this frequency. For higher frequencies, discrepancies between the homogenization levels are visible. Higher homogenization levels show spurious oscillations. In the case with a linear material model, the discrepancies are created due to numerical dispersion. A clear phase shift is noticeable. In this case, with the cubic material model, a phase shift is not visible.

In Figure 6.7, a comparison between the DNS and computational homogenization simulation with an homogenization level of $h = 1$ with the Bathe scheme is shown. At the first few unit cells, the homogenization simulation is not accurate. The homogenization simulation over predicts the displacements in these first few unit cells by an enormous amount. Halfway the system, the fluctuations in the CH simulations are disappearing and the two simulations match. The same results are obtained with the trapezoidal rule and the Wen scheme. The integration scheme does not have any influence on this behaviour. However, the fluctuations are likely caused by the microscale simulations where in all three cases the trapezoidal rule is used.

Figure 6.8 shows a comparison between the displacement of the upper epoxy part for a homogenization level of $h = 12$ and $h = 20$ with the Bathe scheme. From the figure it can be concluded that no clear phase shift can be seen and that the response is chaotic. In the figure only the Bathe scheme is given. However, all three schemes show the same discrepancies between the homogenization levels. Since the trapezoidal rule is used on the microscopic scale, the exact influence of the composite time integration schemes are hard to predict. However, in the DNS results similar fluctuations for the first few unit cells is seen for all three schemes. In the DNS results, the influence of the time integration scheme is minimal, and the expectation is that this will also be the case for the computational homogenization results with a composite time integration scheme at the microscale.

In previous work [5], the cause of these fluctuations are linked to the mismatch in initial and boundary condition. This effect, may introduce a perturbation to the system which the homogenization inaccurately predicts.

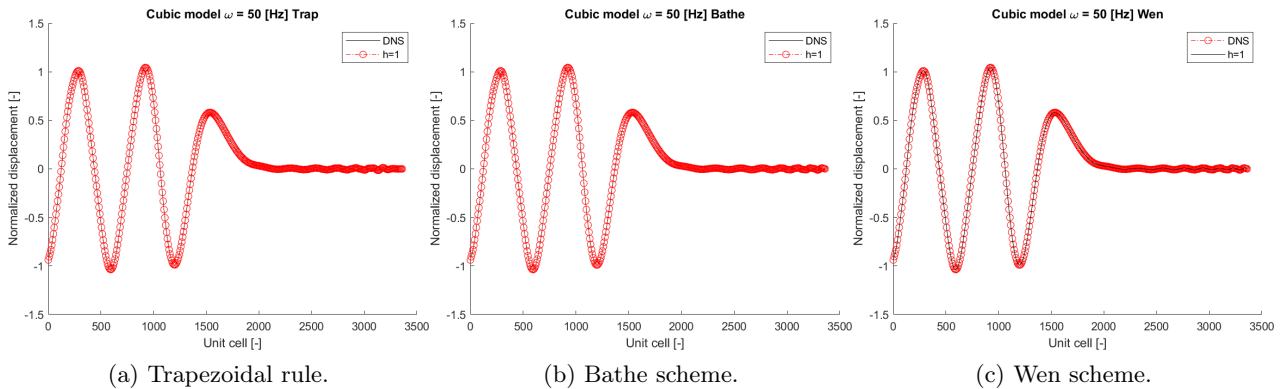


Figure 6.6: Comparison between the displacement for a frequency below the band gap for (a) the trapezoidal rule, (b) the Bathe scheme and (c) the Wen scheme. The displacement is taken at $t = 0.074$ s before the wave reached the end of the system.

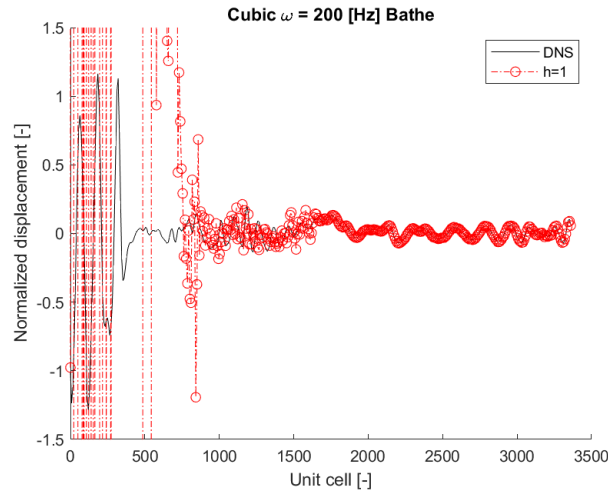


Figure 6.7: Comparison of the displacement of the epoxy node at an input frequency of $\omega = 200$ Hz between the DNS and computational homogenization simulation with an homogenization level of $h = 1$ at $t = 0.054$ s with the Bathe scheme. The top and bottom part is cut-off to increase clarity. The displacement of the CH simulation reaches at the highest point a normalized displacement of 3000.

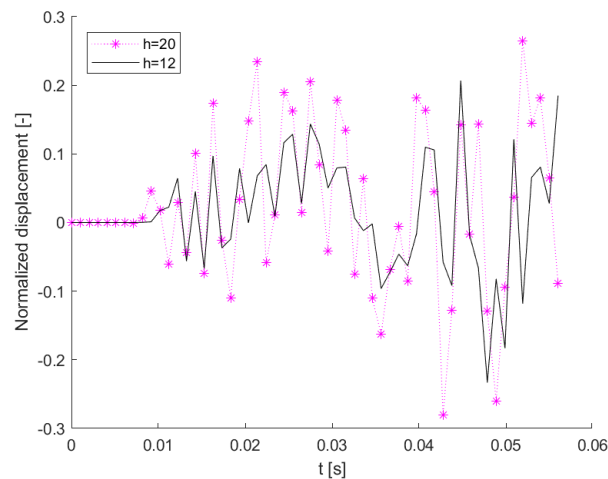


Figure 6.8: Comparison between the displacement of the epoxy part for a homogenization level of $h = 12$ and $h = 20$ at $x = \frac{1}{4}l_M$ with the Bathe scheme for an input frequency of 200 Hz.

6.3 Neo-Hookean

Since the DNS simulations with the Neo-Hookean material model showed unrealistic values for input frequency inside and above the band gap, only a validation is shown for an input frequency below the band gap. Figure 6.9 shows this validation for an input frequency of $\omega = 50$ Hz for the three considered schemes between the DNS and the computational homogenization simulation with an homogenization level $h = 1$. For this frequency, the simulations are equal and no difference between the schemes is observed. Furthermore, a simulation with a higher homogenization level is capable of predicting the same displacement as the DNS simulations.

Comparisons for an input frequency inside or above the band gap can be made when the model is more stable, for instance, by decreasing the applied amplitude of the wave or add numerical damping to the system.

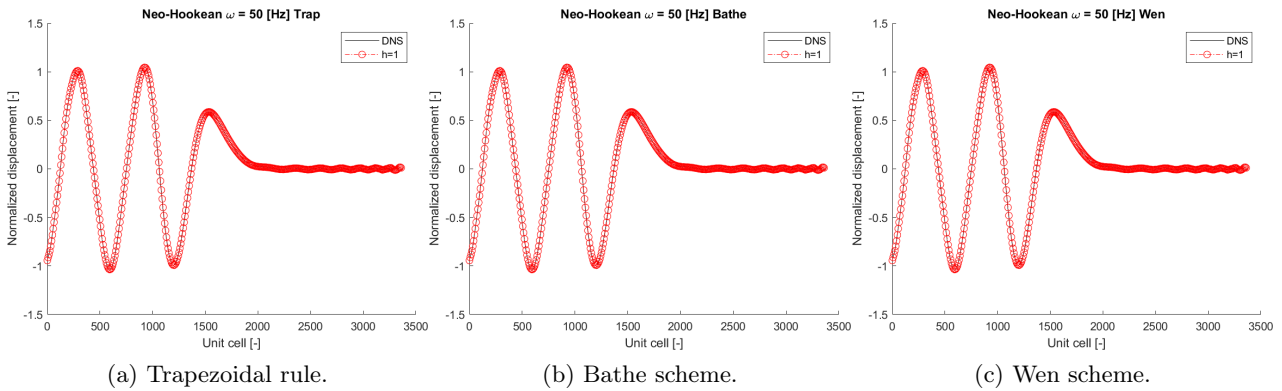


Figure 6.9: Comparison between the displacement for a frequency below the band gap for (a) the trapezoidal rule, (b) the Bathe scheme and (c) the Wen scheme. The displacement is taken at $t = 0.054$ s before the wave reached the end of the system.

6.4 Quadratic elements

Quadratic elements on the microscopic scale showed no influence, as described in the previous chapter. Quadratic elements on the macroscopic scale is expected to have a large influence, especially for high homogenization levels h . In literature (see e.g. [11, 32]), the spatial discretization is heavily discussed for wave propagations, resulting in the importance of higher order elements to increase the accuracy of the model and decrease the numerical dispersion. In the simulations with linear elements, numerical dispersion is found to be the cause of discrepancies between the results with different homogenization levels.

Figures 6.10, 6.11 and 6.12 show the displacement for the DNS and several homogenization simulations for the three considered frequencies for the trapezoidal rule, Bathe scheme and Wen scheme, respectively. These figures show that no difference in the steady state between the different homogenization levels can be seen. Also the schemes are similar and no difference is noticeable in the steady-state region. Where the results with linear elements showed numerical dispersion for higher frequencies, the quadratic elements do not show this. In Figure 6.13, the same plot is shown as in Figure 6.5 but now with quadratic elements. The figures show that the numerical dispersion is gone and the results are equal. This is the case for all considered frequencies.

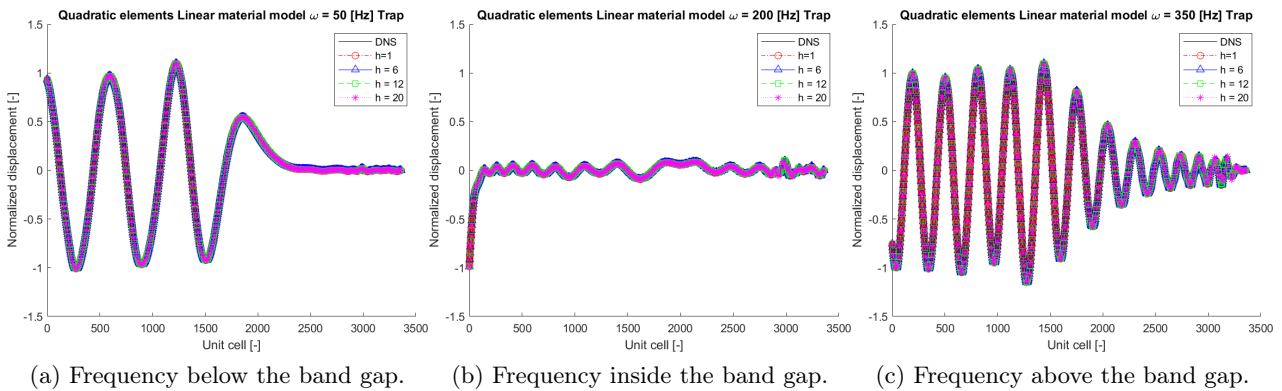


Figure 6.10: Comparison between the displacement via the trapezoidal rule for frequencies below the band gap, above the band gap and above the band gap. The displacement is taken at (a) $t = 0.074$ s, (b) $t = 0.064$ s and (c) $t = 0.054$ s, before the wave reached the end of the system.

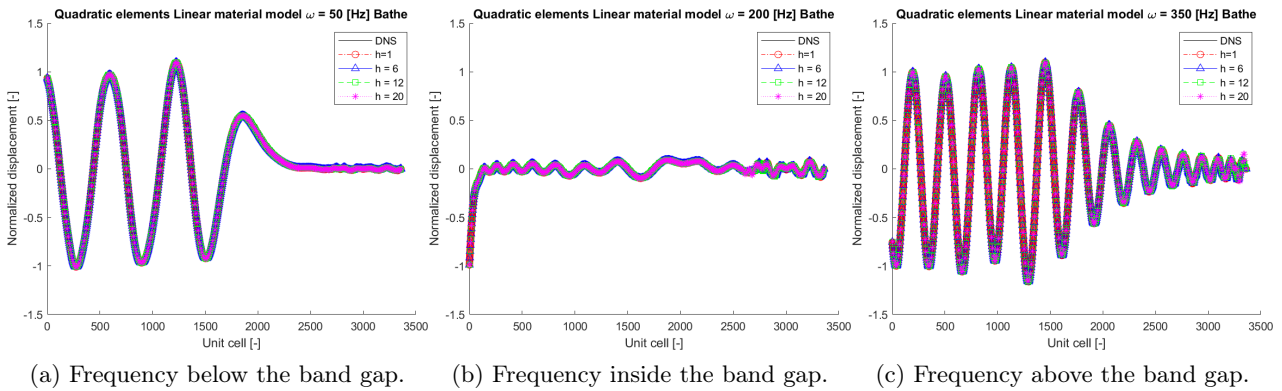


Figure 6.11: Comparison between the displacement via the Bathe scheme for frequencies below the band gap, above the band gap and above the band gap. The displacement is taken at (a) $t = 0.074$ s, (b) $t = 0.064$ s and (c) $t = 0.054$ s, before the wave reached the end of the system.

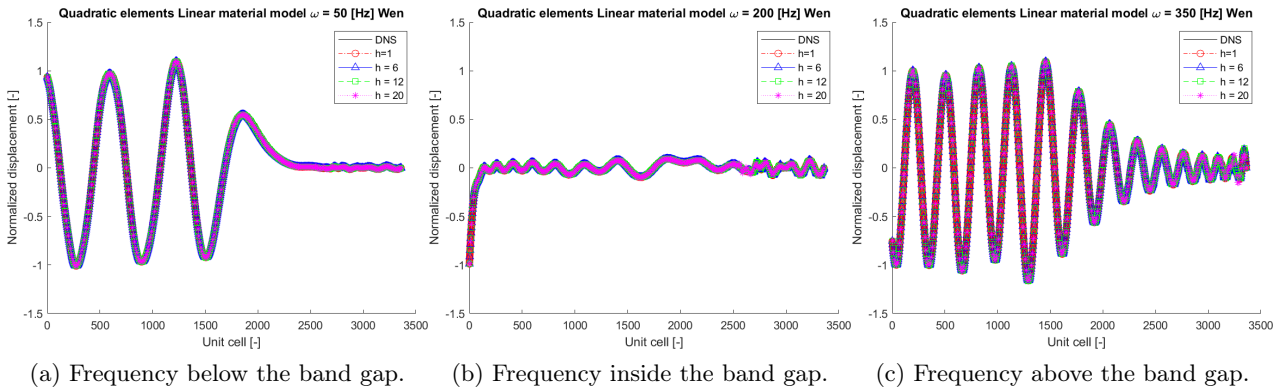


Figure 6.12: Comparison between the displacement via the Wen scheme for frequencies below the band gap, above the band gap and above the band gap. The displacement is taken at (a) $t = 0.074$ s, (b) $t = 0.064$ s and (c) $t = 0.054$ s, before the wave reached the end of the system.

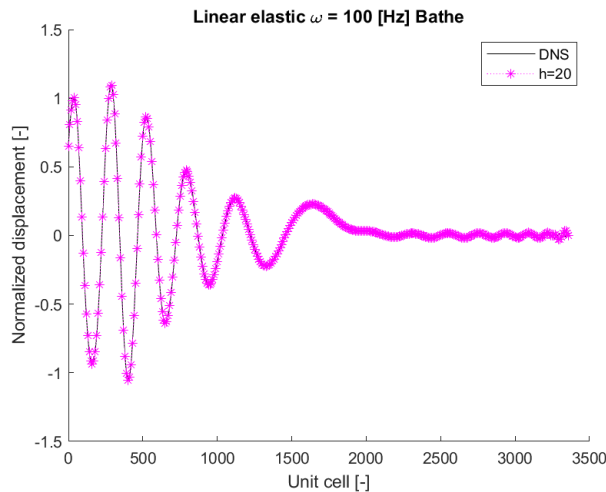


Figure 6.13: Comparison between the DNS and homogenization results with quadratic elements for $h = 20$, with an input frequency of $\omega=100$ Hz in the (a) space domain at $t = 0.074$ s for the Bathe scheme.

6.5 Discussion

A phase shift is observed for high homogenization levels in CH simulation with the linear elastic material model and linear elements. This phase shift (or more general; numerical dispersion) is widely studied in literature for wave propagations. Noh et al. [32] analysed the dispersion due to spatial and temporal discretization for the trapezoidal rule and the Bathe scheme. Noh et al. found that the numerical dispersion is influenced by both discretizations. The discretizations are linked via a CFL (Courant-Friedrichs-Lewy [34]) number which relates the spatial discretization to the temporal discretization as:

$$CFL = \frac{c\Delta t}{\Delta x}, \quad (6.1)$$

where c is the (numerical) wave velocity and Δx is the element length. Noh et al. describes that the trapezoidal rule shows non-dispersive solutions when the wave modes with $k\Delta x < 2$ are considered, where k is the wave number ($k = 2\pi/\Lambda$). However, wave modes with $k\Delta x > 2$ are dispersive since they are not damped out. Since the wave velocity is changing in the LRAM, all three scheme show a non-dispersive part and a dispersive part in the LRAM solution.

Noh et al. also describes the same property for the Bathe scheme, however, in the Bathe scheme, wave modes with $\Delta t/T$, where T is the wave period, are discarded in the numerical solution due to numerical damping [27, 32]. In particular, for a CFL number of 1, the Bathe scheme solves accurately and the solution is almost non-dispersive for the discussed model problems. A lower CFL number results in less discarded wave modes and a higher positive relative wave speed error due to the dispersion. Therefore the numerical wave speed is higher. When a lower CFL number is used, the relative wave speed error is negative resulting in a lower numerical wave speed since more wave modes are discarded.

The Wen scheme shows similar results to the Bathe scheme - where high frequency modes are essentially discarded and the solution is almost non-dispersive - when the CFL equals 1.5 [10].

In the LRAM model, the numerical wave speed in the band gap is a function of the frequency. Therefore, the CFL cannot be determined a priori since it is not known how much the wave propagates. Optimising the CFL number by changing the time step to only include non-dispersive solutions is therefore a hard task. The increase in polynomial order of the shape functions used in the finite element method is a much simpler task. The change from linear to quadratic elements showed that for the linear case the solution becomes non-dispersive and equal to the DNS results for all considered homogenization levels. Note that by increasing the order of the elements, the Δx does not change.

The effect of the time integration schemes are minimal when an input frequency inside the band gap is used, since throughout the model different wave speeds are present. All three schemes show a dispersive part in the solution since the CFL number varies throughout the model. To gain non-dispersive solution with the composite schemes, the time discretization or spatial discretization should also be variable depending on how much the wave is propagating in each unit cell. This is not feasible in the current implementation of the model.

Chapter 7

Conclusions and recommendations

In this work the effect of implicit time integration on the Direct Numerical Simulations (DNS) and computational homogenization framework of locally resonant acoustic metamaterials is analysed. Standard and so-called composite implicit time integration schemes are discussed and the different properties of these schemes are compared. Composite schemes contain sub steps where different standard schemes are used to gain unique properties. An example is using a dissipative and non-dissipative scheme such that the dissipation can be controlled. Three schemes are selected; the trapezoidal rule, the Bathe scheme and the Wen scheme. The three considered schemes are used to solve a model problem to familiarize with the schemes, their implementation and to highlight the different properties. The model problem showed that the trapezoidal rule shows high frequency spurious modes in the velocity and acceleration due to the non-dissipative property. Both the Bathe and Wen scheme do not show spurious oscillations since these schemes have numerical damping incorporated. However, in the first step for the accelerations, the Bathe and the Wen scheme show inaccuracies.

The three considered time integration schemes are used on the DNS and computational homogenization framework. The computational homogenization framework proposed in previous work is used. In this framework, dynamical effects such as micro-inertia are included which are necessary to model the local resonator present in acoustic metamaterials. The computational homogenization framework uses two scales; the macroscale and the microscale. At each macroscopic point, the required quantities are obtained from the microscale simulations. The microscale is described in detail by means of a unit cell. Both scales are discretized by finite elements. The balance of momentum is used to construct the system of equations for which the time integration schemes are used to solve them.

In this work, a one dimensional system is considered. The unit cell consists of a rubber coated lead core, embedded in an epoxy matrix. Three material models describing the rubber material behaviour are considered; linear elastic, cubic and Neo-Hookean. The results obtained with the computational homogenization framework are compared to the DNS results. The DNS simulation consists of a fully spatial resolved dynamic finite element method. The validation is performed for a computational homogenization model containing an equal amount of integration points as the number of unit cells used in the DNS simulation. The simulations are performed for all constitutive models for three frequencies; below, inside and above the band gap. It is expected that these results are equal. By coarsening of the macroscopic scale, less integration points are used resulting in less microscopic simulation.

The use of composite time integration schemes in the computational homogenization framework introduces challenges. Since the time step in the macroscale and microscale can be desynced, the application of the boundary condition is defined differently. In this project, the correct application of boundary condition when using a composite time integration scheme, has not been found. Therefore, in the computational homogenization simulations, the trapezoidal rule is used in the microscale. In the macroscale, the three considered time integration schemes are used.

In the case of linear elastic locally resonant acoustic metamaterial (LRAM), the wave response predicted

via the three schemes are similar in both the DNS and computational homogenization simulations. The velocity and acceleration show high frequency spurious oscillations with the use of the trapezoidal rule. However, these spurious oscillations do not translate to the displacements. Also, the three schemes show the same amount of numerical dispersion when a high homogenization level is used. The numerical damping present in the Bathe and Wen scheme do not result in more accurate results. Since the composite schemes are only used at the macroscopic scale, the exact influence on the microscale is unclear. However, when comparing the obtained results with the DNS simulations where the composite schemes are used, no difference in displacement is seen. The composite schemes predict the wave as accurate as the trapezoidal rule. The numerical dispersion can be decreased by increasing the polynomial order of the finite element interpolation. The use of quadratic elements decreases the numerical dispersion significantly for all three schemes. However, to gain a non-dispersive solution with the composite schemes, the temporal or spatial discretization should be adjustable depending on how much the wave is propagating through the unit cell, which is not feasible with the current implementation.

In future work it is recommended to implement the composite time integration at the microscopic scale. Since the macroscopic quantities are dependent on the microscopic accelerations, the use of composite schemes, where the accelerations show less high frequency spurious modes, can be advantageous. Furthermore, the use of using higher-order polynomials is recommended. The numerical dispersion is codependent on the spatial discretization. Spectral elements make use of higher order polynomials with non-uniformly spaced nodes. This method is known to increase the accuracy in wave propagation problems [35]. Another method is the use of an enriched finite element method where nodes are overlapping. This method combines the key aspect of the spectral method with the standard finite element method to increase the accuracy of wave propagation [36].

In the case of non-linear LRAMs (by using the cubic or Neo-Hookean material model), the use of the composite time integration schemes show differences compared to the trapezoidal rule. When the cubic material model is used, large fluctuations are observed in the first few time steps. These fluctuations are caused by the mismatch in initial and boundary conditions. The time integration schemes are unable to accurately describe these fluctuations resulting in different wave predictions. The composite schemes overestimate the response in the first few unit cells which causes a higher transmissibility. The lack of numerical damping in the Neo-Hookean material model, results in instabilities. The time step must be chosen very small to reach convergence. However, even when convergence is reached, the model shows unrealistic displacements at frequencies inside the band gap for all three schemes. By increasing the homogenization level, numerical dispersion is introduced which causes discrepancies in the results. For the simulations where the results are realistic, all three schemes are similar. Since the effect of the composite time integration schemes for the linear and cubic material model are limited, the expectation is that this is also the case for the Neo-Hookean material model.

In future work it is recommended to decrease the applied amplitude of the input wave to increase the numerical stability for non-linear material models or add numerical damping to the system.

Bibliography

- [1] Y. Ding, Z. Liu, C. Qiu, and J. Shi. Metamaterial with simultaneously negative bulk modulus and mass density. *Physical Review Letters*, 99(9):093904, 8 2007.
- [2] J. Mei, G. Ma, M. Yang, J. Yang, and P. Sheng. Dynamic Mass Density and Acoustic Metamaterials. *Physica B*, 394:256–261, 2007.
- [3] A. O. Krushynska, V. G. Kouznetsova, and M. G.D. Geers. Towards optimal design of locally resonant acoustic metamaterials. *Journal of the Mechanics and Physics of Solids*, 71(1):179–196, 2014.
- [4] Younes Achaoui, Bogdan Ungureanu, Stefan Enoch, Stéphane Brûlé, and Sébastien Guenneau. Seismic waves damping with arrays of inertial resonators. *Extreme Mechanics Letters*, 8:30–37, 9 2016.
- [5] T.F.W. van Nuland. *Computational Homogenization of Acoustic Metamaterials with nonlinear locally resonant material behaviour (MSc Thesis)*. 2017.
- [6] T. F.W. van Nuland, P. B. Silva, A. Sridhar, M. G.D. Geers, and V. G. Kouznetsova. Transient analysis of nonlinear locally resonant metamaterials via computational homogenization. *Mathematics and Mechanics of Solids*, 24(10):3136–3155, 10 2019.
- [7] Z. Liu, X. Zhang, Y. Mao, Y. Y. Zhu, Z. Yang, C. T. Chan, and P. Sheng. Locally resonant sonic materials. *Science*, 289(5485):1734–1736, 9 2000.
- [8] N. M. Newmark. A method of computation for structural dynamics. *Journal of the Engineering Mechanics Division*, 85(3):67–94, 1959.
- [9] K.J. Bathe. Conserving energy and momentum in nonlinear dynamics: A simple implicit time integration scheme. *Computers and Structures*, 85(7-8):437–445, 4 2007.
- [10] W. B. Wen, K. Wei, H. S. Lei, S. Y. Duan, and D. N. Fang. A novel sub-step composite implicit time integration scheme for structural dynamics. *Computers and Structures*, 182:176–186, 4 2017.
- [11] Sun Beom Kwon, Klaus Jürgen Bathe, and Gunwoo Noh. An analysis of implicit time integration schemes for wave propagations. *Computers and Structures*, 230, 4 2020.
- [12] Steen Krenk. Energy conservation in Newmark based time integration algorithms. *Computer Methods in Applied Mechanics and Engineering*, 195(44-47):6110–6124, 9 2006.
- [13] A. Iserles. *A first course in the numerical analysis of differential equations, second edition*. Cambridge University Press, 1 2008.
- [14] G. Noh and K. J. Bathe. For direct time integrations: A comparison of the Newmark and q 1-Bathe schemes. 2019.
- [15] L. Euler. *Institutionum calculi integralis volumen primum*, volume II. Imperial Academy of Sciences, St. Petersburg, 1768.

- [16] W. Wen, Y. Tao, S. Duan, J. Yan, K. Wei, and D. Fang. A comparative study of three composite implicit schemes on structural dynamic and wave propagation analysis. *Computers and Structures*, 190:126–149, 10 2017.
- [17] Y. Chandra, Y. Zhou, I. Stanciulescu, T. Eason, and S. Spottswood. A robust composite time integration scheme for snap-through problems. *Computational Mechanics 2015 55:5*, 55(5):1041–1056, 4 2015.
- [18] G.M. Hulbert and J. Chung. A time integration algorithm for structural dynamics with improved numerical dissipation: The Generalized-alpha Method. *Journal of Applied Mechanics*, 60:371–375, 1993.
- [19] C. F. Curtiss and J. O. Hirschfelder. Integration of stiff equations. *Proceedings of the National Academy of Sciences*, 38(3):235–243, 3 1952.
- [20] J. Li and K. Yu. An alternative to the Bathe algorithm. *Applied Mathematical Modelling*, 69:255–272, 5 2019.
- [21] C.W. Gear. *Numerical initial value problems in ordinary differential equations*. Prentice Hall PTR, 1971.
- [22] J. Li, X. Li, and K. Yu. Enhanced studies on the composite sub-step algorithm for structural dynamics: The Bathe-like algorithm. *Applied Mathematical Modelling*, 80:33–64, 4 2020.
- [23] J. C. Houbolt. A recurrence matrix solution for the dynamic response of elastic aircraft. *Journal of the Aeronautical Sciences*, 17(9):540–550, 9 1950.
- [24] W. Kim. An improved implicit method with dissipation control capability: The simple generalized composite time integration algorithm. *Applied Mathematical Modelling*, 81:910–930, 5 2020.
- [25] S. Dong. BDF-like methods for nonlinear dynamic analysis. *Journal of Computational Physics*, 229(8):3019–3045, 4 2010.
- [26] I. Gladwell and R. Thomas. Stability properties of the Newmark, Houbolt and Wilson θ methods. *International Journal for Numerical and Analytical Methods in Geomechanics*, 4(2):143–158, 4 1980.
- [27] K. J. Bathe and G. Noh. Insight into an implicit time integration scheme for structural dynamics. *Computers and Structures*, 98-99:1–6, 5 2012.
- [28] J. Li, K. Yu, and H. He. A second-order accurate three sub-step composite algorithm for structural dynamics. *Applied Mathematical Modelling*, 77:1391–1412, 1 2020.
- [29] K. Bathe. *Finite Element Procedures Second Edition Bathe Finite Element Procedures*. Second edition edition, 2006.
- [30] T. van Loon. *Analysis of the wave propagation in chains with various non-linear attached resonators*. PhD thesis, Eindhoven University of Technology, 2016.
- [31] F. Ihlenburg and I. Babuška. Dispersion analysis and error estimation of Galerkin finite element methods for the Helmholtz equation. *International journal for numerical methods in engineering*, 38:3745–3774, 1995.
- [32] G. Noh, S. Ham, and K. J. Bathe. Performance of an implicit time integration scheme in the analysis of wave propagations. *Computers and Structures*, 123:93–105, 2013.

-
- [33] P.B. Silva, M.J. Leamy, M.G.D. Geers, and V.G. Kouznetsova. Emergent subharmonic band gaps in nonlinear locally resonant metamaterials induced by autoparametric resonance. *Phys. Rev. E*, 99(6), 2019.
- [34] R. Courant, K. Friedrichs, and H. Lewy. Über die partiellen Differenzgleichungen der mathematischen Physik. *Mathematische Annalen*, 100(1):32–74, 12 1928.
- [35] D. Gottlieb and S.A. Orszag. *Numerical Analysis of Spectral Methods: Theory and Applications*. Capital City Press, 19793.
- [36] Seounghyun Ham and Klaus-Jürgen Bathe. A finite element method enriched for wave propagation problems. 2012.

Chapter 8

Appendix A: Finite element method

The Finite Element Method (FEM) also makes use of a discrete system (of elements). The difference between the discrete system described in Chapter 3 and FEM is that the latter uses shape functions to interpolate between nodes where the solution is computed such that the solution is determined over the entire domain. The other method only calculates the solution at specific points without interpolation. In this work, two element types are adopted, linear and quadratic. The linear shape functions \mathbf{N}_e are expressed as:

$$\mathbf{N}_e(\xi) = \begin{bmatrix} \frac{1}{2}(1 - \xi) \\ \frac{1}{2}(1 + \xi) \end{bmatrix}, \quad \nabla_\xi = \begin{bmatrix} -\frac{1}{2} \\ \frac{1}{2} \end{bmatrix}, \quad (8.1)$$

where ∇_ξ is the derivative of the shape functions with respect to the local coordinate ξ . Quadratic shape functions require an extra node in each element. Therefore, the solution is more accurate but it requires more computational cost when the same number of elements are used. The quadratic shape functions and their derivatives are expressed as:

$$\mathbf{N}_e(\xi) = \begin{bmatrix} -\frac{1}{2}(1 - \xi)\xi \\ 1 - \xi^2 \\ \frac{1}{2}(1 + \xi)\xi \end{bmatrix}, \quad \nabla_\xi = \begin{bmatrix} \xi - \frac{1}{2} \\ -2\xi \\ \xi + \frac{1}{2} \end{bmatrix}. \quad (8.2)$$

The shape functions are used to construct the elemental stiffness matrix \mathbf{K}_e , elemental mass matrix \mathbf{M}_e , and the elemental internal forces $\mathbf{f}_{int,e}$ as:

$$\mathbf{K}_e = \sum_{p=1}^q w_p \nabla_0 \mathbf{N}_e k_e (\nabla_0 \mathbf{N}_e)^T J_0, \quad (8.3)$$

$$\mathbf{M}_e = \sum_{p=1}^q w_p \mathbf{N}_e \rho_e \mathbf{N}_e^T J_0, \quad (8.4)$$

$$\mathbf{f}_{int,e} = \sum_{p=1}^q w_p \nabla_0 \mathbf{N}_e P_e J_0, \quad (8.5)$$

where w_p are the weights of integration point p and J_0 is the Jacobian with respect to the initial configuration, which is expressed as:

$$J_0(\xi) = \nabla_\xi \mathbf{N}_e^T \mathbf{X}_{0,e}, \quad (8.6)$$

and with,

$$\nabla_0 \mathbf{N}_e = J_0^{-1} \nabla_\xi \mathbf{N}_e. \quad (8.7)$$

In these equations, the subscript 0 refers to the initial configuration (also commonly referred to as total Lagrange), subscript e is for element e and the summation is for each integration point p to all

integration points q . The stiffness contribution k_e , density ρ_e and stress P_e depend on the constitutive relation.

Now that the elemental contributions \mathbf{K}_e , \mathbf{M}_e and $\mathbf{f}_{int,e}$ for each element e are computed, the global system can be assembled:

$$\mathbf{K} = \sum_{e=1}^m \mathbf{K}_e, \quad \mathbf{M} = \sum_{e=1}^m \mathbf{M}_e, \quad \mathbf{f}_{int} = \sum_{e=1}^m \mathbf{f}_{int,e}, \quad (8.8)$$

where m is the total number of elements. Now that the stiffness matrix, mass matrix and the internal forces are constructed, the time integration can be performed. To solve the governing Equation 2.2, the procedure is exactly the same as described in Table 2.4 and 2.5 for the standard scheme and composite scheme, respectively.